Self-organized error correction in random unitary circuits with measurement

Ruihua Fan, Sagar Vijay, Ashvin Vishwanath, and Yi-Zhuang You

Self-Organized Error Correction in Random Unitary Circuits with Measurement

Ruihua Fan,[1] Sagar Vijay,[2, 1] Ashvin Vishwanath,[1] and Yi-Zhuang You[3]

[1] Department of Physics, Harvard University, Cambridge, MA 02138, USA
[2] Department of Physics, University of California, Santa Barbara, CA 93106, USA
[3] Department of Physics, University of California, San Diego, La Jolla, CA 92093, USA

Random measurements have been shown to induce a phase transition in an extended quantum system evolving under chaotic unitary dynamics, when the strength of measurements exceeds a threshold value. Below this threshold, a steady-state with a sub-thermal volume law entanglement emerges, which is resistant to the disentangling action of measurements, suggesting a connection to quantum error-correcting codes. We quantify these notions by identifying a power-law decay of the mutual information $I(\{x\} : \bar{A}) \propto x^{-3/2}$ in the volume-law-entangled phase, between a qudit located a distance x from the boundary of a region A, and the complement $\bar{A}$, which implies that a measurement of this qudit will retrieve very little information about $\bar{A}$. We also find a universal logarithmic contribution to the volume law entanglement entropy $S^{(2)}(A) = \kappa L_A + \frac{3}{2} \log L_A$ which is intimately related to the first observation. We obtain these results by relating the entanglement dynamics to the imaginary time evolution of an Ising model, to which we apply field-theoretic and matrix-product-state techniques. Finally, exploiting the error-correction viewpoint, we assume that the volume-law state is an encoding of a Page state in a quantum error-correcting code to obtain a bound on the critical measurement strength p_c as a function of the qudit dimension d: $p_c \log[(d^2 - 1)(p_c^{-1} - 1)] \leq \log[(1 - p_c)d]$. The bound is saturated at $p_c(d \to \infty) = 1/2$ and provides a reasonable estimate for the qubit transition: $p_c(d = 2) \leq 0.1893$.

Introduction— The study of random unitary circuits has significantly advanced our understanding of the universal behavior of entanglement and operator dynamics in quantum many-body systems[1–12]. Locally accessible quantum information becomes scrambled under unitary evolution[13, 14], which typically leads to thermalization, accompanied by volume-law scaling of the entanglement entropy[15] in the steady-state. This is consistent with the idea that entropy should be an extensive property for thermal systems[16, 17]. It has been recently found that performing local measurements along with random, local unitary dynamics can slow down and stop thermalization. Conditioned on the measurement outcome, the qubit that has been measured will be projected to a product state, and disentangled from the rest of the system. When the measurement rate is high enough, most qubits in the system will be disentangled, and the final state will exhibit area-law entanglement scaling[18–20], a manifestation of the quantum Zeno effect[21]. Driven by the measurement rate, the final state of this quantum channel (i.e. the quantum circuit with measurements) exhibits an entanglement phase transition driven by the measurement rate [21–23], which has attracted much recent interest[24–32].

Progress has been made in understanding this transition by mapping the problem to the statistical mechanics model of permutation group elements[23–25, 33], where the entanglement transition between the volume-law and area-law phases corresponds to the ordering transition in this classical lattice "magnet". The universality of the entanglement transition remains to be fully understood, due to the difficulty in taking the required replica limit[24, 25] of the statistical mechanics model.

In this work, we turn our attention away from the transition point to focus on features of the volume-law phase. Specifically, what are the key, quantitative properties of the volume-law phase that ensure its stability against local measurements? To answer this question, we propose a "mean-field" description for the measurement-induced entanglement transition based on the recently developed entanglement feature formulation for locally scrambled quantum dynamics[34], which is in line with the statistical mechanics description of quantum many-body entanglement[35–37]. This mean-field description cannot provide a precise description of the critical fluctuations at the transition point; nevertheless, we argue that it captures the asymptotic entanglement properties away from the transition. The entanglement feature formalism provides a powerful tool for studying unitary dynamics with measurements. Within this formulation, the mean-field description of the evolution of the second Rényi entropy is Markovian, as it only relies on the second Rényi entropies for all sub-systems in the previous timestep of the evolution. These entanglement dynamics can be further related to the Floquet dynamics of an Ising model, whose steady-state properties can be determined by well-developed theoretical and numerical methods.

Using this solution, we show that the reduction of the entanglement entropy for a contiguous subsystem after performing a measurement decays as a power-law in the distance of the measurement position from the region's boundary with an exponent 3/2. This exponent being larger than 1 is a direct explanation of the stability of the volume-law phase. It follows from our formalism that the mutual information between a qudit inside the subsystem and the exterior decays with the distance from the subsystem's boundary in the same power-law fashion. This exponent does not change as long as the system is deep in the volume-law phase. We also performed a large-scale

numerics with a certain random Clifford circuit and observe a clear power-law decay of the mutual information which appears quantitatively close to the "mean-field" results . A further analytical calculation shows that this power-law decay is intimately related to a logarithmic sub-leading scaling for the entanglement entropy, which was first identified in numerical studies of Clifford dynamics with measurements by Ref. [26], and was conjectured to be a defining feature of the volume-law phase. Here, we calculate the coefficient of this subleading factor analytically and show it to be a universal number $\delta = 3/2$ deep in the volume law phase. In Ref. [26], this coefficient was found to be $\delta \sim 1.06$, albeit near the critical point. Verifying this second observation in large-scale numerics with Clifford circuits requires fitting and is tricky to implement, we do not provide independent check as we have for the power-law decay. These features suggest the quantum error correction (QEC) properties of these volume-law states, which accounts for their stability against local measurements. By quantitatively studying the error-correcting properties of the final state, we also derive a bound (11) on the measurement rate as a function of the local Hilbert space dimension, above which the system must be in an area-law entangled phase. In previous work [27, 28], other perspectives that relate the entanglement phase transition to QEC have been discussed.

Random Quantum Channel Model— We consider the quantum dynamics of a 1D array of N qudits, each with Hilbert space dimension d. The quantum dynamics is modeled by a random unitary circuit with random measurements implemented uniformly, as shown in Fig. 1. The circuit consists of two-qudit unitary gates $U_{ij,t}$ (acting on qudits i, j at layer t) arranged in a brick-wall pattern. All gates are drawn from the Haar random unitary ensemble independently throughout space and time. After each layer of the unitary gates, measurements are carried out on every qudit. Each single-qudit measurement can be described by the measurement operator $M_{i,t}$ (acting on qudit i at layer t)[38, 39], which is independently drawn from the ensemble $\{\mathbb{I}\} \cup \{\sqrt{d}P_V | V \in U(d)\}$ with the probability measure $P(\mathbb{I}) = 1 - p$ and $P(\sqrt{d}P_V) = p \, dV$ (with dV being the Haar measure)[25], where $P_V = V |0\rangle \langle 0| V^\dagger$ represents a random projector in the qudit Hilbert space. This ensemble can model either a projective measurement[21, 23] happening with probability p or a weak measurement[24] with strength p. Both the unitary operator $U_{ij,t}$ and the measurement operator $M_{i,t}$ can be generally denoted as the Kraus operator $K_{x,t}$ at different spacetime positions labeled by (x, t) in general. They together form the quantum channel, described by the overall Kraus operator $K = \prod_t \prod_x K_{x,t}$, such that the density matrix ρ of the quantum system evolves by the completely positive trace-preserving map $\rho \to K\rho K^\dagger / \text{Tr}(K\rho K^\dagger)$ under the quantum dynamics. Strictly speaking, our protocol is different from doing physical measurement. The latter also involves postselection based on the probability of possible outcomes. In the volume-law phase, local scrambling and the low-density of measurements implies that the probability of each outcome is identical and the two protocols are expected to yield similar results. (See Appendix A for detailed verification)[40]
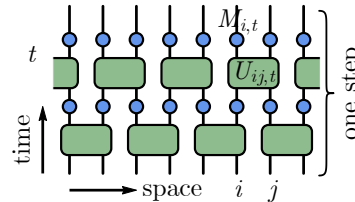

FIG. 1. The random quantum channel model. Green blocks are two-qudit Haar random unitary gates. Blue dots are single-qudit random measurements (which can be either weak measurements or projective measurements with probability).

Entanglement Feature Formalism— We are interested in the purity of the reduced density matrix $\rho_A = \text{Tr}_{\bar{A}} \rho$ over all possible subsystem A,

$$W_\rho(A) = \text{Tr} \, \rho_A^2 = e^{-S_\rho^{(2)}(A)}. \tag{1}$$

It is directly related to the 2nd Rényi entanglement entropy $S_\rho^{(2)}(A)$ that quantifies the amount of quantum entanglement between A and $\bar{A}$ in the state ρ (assuming ρ is pure). To organize this purity data in a more concise way, we introduce a set of Ising variables $[\sigma] \equiv [\sigma_1, \sigma_2, \cdots, \sigma_N]$ to label the subsystem A, s.t. $\sigma_i = -1 \, (\downarrow)$ if $i \in A$ and $\sigma_i = +1 \, (\uparrow)$ if $i \in \bar{A}$. Then $W_\rho(A)$ can be written as[7, 34]

$$W_\rho[\sigma] = \text{Tr} \, \rho^{\otimes 2} \mathcal{X}_\sigma, \tag{2}$$

where $\mathcal{X}_\sigma = \prod_i \mathcal{X}_{\sigma_i}$ is a string of identity $\mathcal{X}_{\sigma_i=\uparrow} \equiv \| $ and swap $\mathcal{X}_{\sigma_i=\downarrow} \equiv \mathsf{X}$ operators acting in the duplicated Hilbert space as specified by the Ising variable σ_i. The collection of $W_\rho[\sigma]$ over all Ising configurations $[\sigma]$ is called the *entanglement feature*[7, 41] of the density matrix ρ, which characterizes all the bipartite entanglement properties of ρ. They can be naturally assembled into a vector

$$|W_\rho\rangle = \sum_{[\sigma]} W_\rho[\sigma] |\sigma\rangle, \tag{3}$$

called the *entanglement feature state*[34], with $|\sigma\rangle$ being a set of orthonormal Ising basis labelled by $[\sigma]$. The normalization $\text{Tr} \, \rho = 1$ implies $\langle \Uparrow | W_\rho \rangle = 1$ for the entanglement feature state, where $|\Uparrow\rangle$ denotes the all-up state ($\forall i : \sigma_i = +1$). Nevertheless, $|W_\rho\rangle$ is still well-defined for unnormalized density matrix ρ following Eq. (2), which will also be useful in our discussion.

As the state ρ evolves under the random quantum channel in Fig. 1, the corresponding entanglement feature

state $|W_\rho\rangle$ also evolves, which defines the entanglement dynamics. Ref. 34 pointed out that if the quantum dynamics is locally scrambled, the corresponding entanglement dynamics is Markovian and admits a transfer matrix description. More precisely, suppose the Kraus operator K is randomly drawn from a local-basis independent ensemble, i.e. the probability $P(K) = P(VKV^\dagger)$ is invariant under arbitrary local (on-site) basis transformation $V = \prod_i V_i$ for $V_i \in U(d)$, then under the completely positive map $\rho_0 \to \rho = K\rho_0 K^\dagger$, the corresponding (ensemble averaged) entanglement feature state evolves as

$$|W_\rho\rangle \equiv \mathop{\mathbb{E}}_{K} |W_{K\rho_0 K^\dagger}\rangle = \hat{W}_K \hat{W}_{\mathbb{I}}^{-1} |W_{\rho_0}\rangle = \hat{T}_K |W_{\rho_0}\rangle, \tag{4}$$

where the *entanglement feature operator* $\hat{W}_K$ associated with a Kraus operator K is defined as[7, 34]

$$\hat{W}_K = \sum_{[\sigma,\tau]} |\sigma\rangle \, W_K[\sigma,\tau] \, \langle\tau|,$$
$$W_K[\sigma,\tau] = \mathrm{Tr}\, K^{\dagger\otimes 2} \mathcal{X}_\sigma K^{\otimes 2} \mathcal{X}_\tau, \tag{5}$$

which captures the entanglement feature of the quantum channel K among its input and output degrees of freedoms. Here, $\hat{W}_{\mathbb{I}}$ is the entanglement feature operator for the identity channel, whose inverse is denoted by $\hat{W}_{\mathbb{I}}^{-1}$. The entanglement dynamics is then determined by the transfer matrix $\hat{T}_K = \hat{W}_K \hat{W}_{\mathbb{I}}^{-1}$, which solely depends on the entanglement property of the quantum channel K.

Mean-Field Description— The random quantum channel model falls in the class of locally scrambled quantum dynamics, for which Eq. (4) applies. However, Eq. (4) only provides the average entanglement feature for the unnormalized state $\rho = K\rho_0 K^\dagger$. For the normalized final state $\bar{\rho} = \rho/\mathrm{Tr}\,\rho$, its average entanglement feature

$$W_{\bar{\rho}}[\sigma] = \mathop{\mathbb{E}}_{K} \mathrm{Tr}\, \bar{\rho}^{\otimes 2} \mathcal{X}_\sigma = \mathop{\mathbb{E}}_{K} \frac{\mathrm{Tr}\, \rho^{\otimes 2} \mathcal{X}_\sigma}{(\mathrm{Tr}\, \rho)^2}, \tag{6}$$

is still difficult to evaluate. Rigorous treatments have been developed using the replica trick[23–25, 33, 42]. Nevertheless, we will approximate the average of ratio in Eq. (6) by the ratio of averages to achieve a simplified "mean-field" description

$$W_{\bar{\rho}}[\sigma] \simeq \frac{\mathbb{E}_K \, \mathrm{Tr}\, \rho^{\otimes 2} \mathcal{X}_\sigma}{\mathbb{E}_K \, \mathrm{Tr}\, \rho^{\otimes 2}} = \frac{W_\rho[\sigma]}{W_\rho[\Uparrow]} = \frac{\langle\sigma|W_\rho\rangle}{\langle\Uparrow|W_\rho\rangle}. \tag{7}$$

In this mean-field treatment, we replace the denominator $(\mathrm{Tr}\, K\rho_0 K^\dagger)^2$ by its expectation value, which ignores both the correlation between the fluctuation of the numerator and denominator and the fluctuation of the denominator itself. The intuition comes from that the random unitary gates are fast local scramblers, i.e. on-site thermalization can be quickly achieved after every layer of unitaries. Consequently, each single qudit should look maximally mixed before the measurement and the trace $\mathrm{Tr}\, M_i \rho_i M_i^\dagger \simeq 1$ is almost independent of the choice of the

measurement operator M_i and the quantum trajectory. (See Appendix A for detailed check) Although our model is set up with Haar random unitaries, the approximation of Eq. (6) by Eq. (7) only requires local scrambling and should also hold for random Clifford circuits. Since the Clifford group is a unitary 2-design [43], this further implies that the dynamics of the purity for the Clifford circuit and Haar random circuit are identical within our formalism.

Now the task is to evaluate the transfer matrix $\hat{T}_K$ for the quantum channel. Because Eq. (4) is applicable to every Kraus operator $K_{x,t}$ in the quantum channel, $\hat{T}_K$ can be constructed from each single $\hat{T}_{K_{x,t}}$ recursively. Following Eq. (5), we find (see Appendix C for derivation)

$$\hat{T}_{U_{ij}} = \left(1 + \frac{d}{d^2+1}(X_i + X_j)\right)\frac{1 + Z_i Z_j}{2},$$
$$\hat{T}_{M_i} = 1 - \frac{p}{d+1} + \frac{pd}{d+1}X_i, \tag{8}$$

where X_i and Z_i denote the Pauli-x and Pauli-z operators acting on site i. Each step of the transfer matrix (see Fig. 1) is then given by

$$\hat{T}_{\mathrm{step}} = \prod_i \hat{T}_{M_i} \prod_{\langle ij\rangle \in \mathrm{even}} \hat{T}_{U_{ij}} \prod_i \hat{T}_{M_i} \prod_{\langle ij\rangle \in \mathrm{odd}} \hat{T}_{U_{ij}}, \tag{9}$$

such that the full transfer matrix of t steps (layers) of the quantum channel will be $\hat{T}_K = \hat{T}_{\mathrm{step}}^t$. According to Eq. (4), the final entanglement feature state reads $|W_\rho\rangle = \hat{T}_{\mathrm{step}}^t |W_{\rho_0}\rangle$, from which the 2nd Rényi entropy in the final state $\bar{\rho}$ can be retrieved based on Eq. (7),

$$S_{\bar{\rho}}^{(2)}[\sigma] = -\log W_{\bar{\rho}}[\sigma] \simeq -\log \frac{\langle\sigma|W_\rho\rangle}{\langle\Uparrow|W_\rho\rangle}, \tag{10}$$

where the Ising configuration $[\sigma]$ labels the entanglement region. The denominator $\langle\Uparrow|W_\rho\rangle$ provides the appropriate normalization to ensure that the entanglement entropy vanishes for empty region, i.e. $S_{\bar{\rho}}^{(2)}[\Uparrow] = 0$. In the long-time limit ($t \to \infty$), the entanglement feature state $|W_\rho\rangle$ converges to the leading eigenvector of the one-step transfer matrix $\hat{T}_{\mathrm{step}}$, denoted as $|W_{\rho_\infty}\rangle$.

Driven by the measurement strength p, the leading eigenstate $|W_{\rho_\infty}\rangle$ can undergo a quantum phase transition that corresponds to the entanglement transition[33]. To see this, we need to calculate $|W_{\rho_\infty}\rangle$ for different p, which is still a challenging many-body problem. An important observation is that the entanglement feature state $|W_\rho\rangle$ itself is a low-entanglement state[44], even if its underlying physical quantum state ρ can be highly entangled. Representing $|W_\rho\rangle$ as a matrix product state (MPS)[45] enables us to tackle the problem using well-developed MPS-based numerical approaches[46–49] (see Appendix D for algorithm details). We assume that the initial physical state ρ_0 is a random product state, whose entanglement feature state is $|W_{\rho_0}\rangle = \sum_{[\sigma]} |\sigma\rangle$, such that
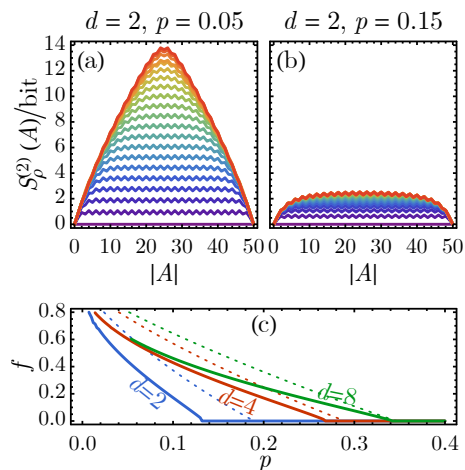
FIG. 2. Growth of entanglement entropy over a single region of size $|A|$ on a chain of 50 qubits in (a) the volume-law phase and (b) the area-law phase. The rainbow colors from purple to red correspond to the time step from 0 to 20. (c) The volume-law coefficient f v.s. the measurement strength p with different qudit dimensions d, where f is extracted in the thermodynamic limit from the MPS representation of $|W_{\rho_\infty}\rangle$ with bond dimension 16. Dash lines are upper bonds of f by the quantum Hamming bound $d^{(1-f)N} \geq \binom{N}{pN}(d^2-1)^{pN}$.

the entanglement entropy $S^{(2)}_{\rho_0}[\sigma] = 0$ vanishes for all entanglement regions. We numerically evolve $|W_{\rho_0}\rangle$ by $\hat{T}_{\text{step}}$ and present the growth and saturation of the entanglement entropy in Fig. 2(a,b). We indeed observe the volume-law (area-law) behavior under small (large) measurement strength. Without the entanglement feature approach, it would be hard to directly simulate the volume-law state in Fig. 2(a) with around 14 bits of half-system entanglement entropy. As the entanglement feature state converges to $|W_{\rho_\infty}\rangle$ in the long-time limit, we can extract the volume-law coefficient f, defined via $S^{(2)}_{\rho_\infty}(A) = (f \log d)|A|$. The result is shown in Fig. 2(c), which clearly exhibits the measurement-driven entanglement transition for different qudit dimensions d, where different curves collapse to the same scaling form $f \log d \propto (p_c-p)^\nu$ with $\nu = 1$ (see Appendix B), implying the Ising universality class within the mean-field description. Nevertheless, the mean-field theory can not capture the universality correctly. Recent numerics indicate that the correct exponent ν should be $1.1 \sim 1.3$[26–29].

Error Correcting Volume-Law States— The result in Fig. 2(c) indicates that the volume-law phase is stable against finite strength of measurements. The volume-law scaling implies that the entropy associated with each qudit is $f \log d$ with $f \leq 1$. If a single-qudit measurement of strength p reduced the qudit entropy by $pf \log d$, then after each layer of measurements, the entropy of a large region A would be reduced in a volume-law manner $\Delta S^{(2)}(A) = -(pf \log d)|A|$, which is irremediable by the

following layer of unitary gates, which only increases the entropy by an area-law amount $\Delta S^{(2)}(A) \propto |\partial A| \sim \mathcal{O}(1)$. This would imply that the volume-law phase is unstable against measurements, a paradox posted in Ref. 22. It was pointed out in Ref. 27 that the solution lies in the QEC [50, 51] property in the sub-thermal volume-law state. An example of such volume-law state on N qudits can be obtained from encoding a Page state of fN qudits by a layer of local QEC code as in Fig. 3(a), which dilutes the Page state to a sub-thermal volume-law state with volume-law coefficient $f \leq 1$. In each round of local measurements, pN qudits will be measured typically, which effectively introduces errors up to weight pN. To prevent the measurement from disentangling the Page state and reducing the entanglement entropy extensively, these errors must be correctable by the subsequent unitary layer (see Appendix E). Assuming the code is non-degenerate[28], this requires the syndrome space dimension $d^{(1-f)N}$ to be at least as large as the number of error operators of weight pN,[52] which yields the quantum Hamming bound[53] $d^{(1-f)N} \geq \binom{N}{pN}(d^2-1)^{pN}$, see Fig. 2(c). The entanglement transition happens as $f \to 0$. In the $N \to \infty$ limit, this gives a bound on the critical measurement rate p_c

$$p_c \log[(d^2-1)(p_c^{-1}-1)] \leq \log[(1-p_c)d], \tag{11}$$

which is plotted in Fig. 3(b). For qubits ($d = 2$), this yields $p_c \leq 0.1893$, the limit of infinite qudit dimension ($d \to \infty$) yields $p_c \leq 1/2$, as summarized in Fig. 3(c). The latter bound is saturated at the known transition point, corresponding to a bond percolation transition on the square lattice [23–25].
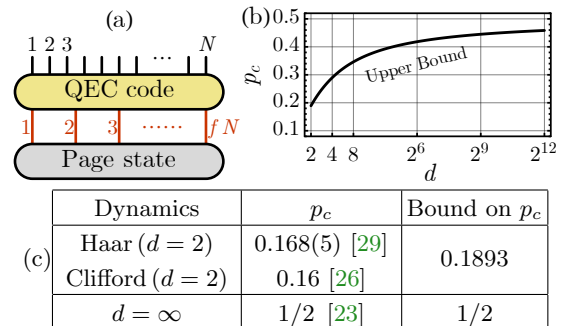

FIG. 3. (a) Assuming the final steady state can be modeled by a Page state on fN qudits ($f \leq 1$) encoded into a quantum error-correcting code on N qudits, we find (b) a upper bound on the critical measurement strength p_c for different qudit dimensions d as in Eq. (11), where $p_c \to 1/2$ as $d \to \infty$. (c) Comparison with p_c reported in literatures.

Dynamics	p_c	Bound on p_c
Haar ($d = 2$)	0.168(5) [29]	0.1893
Clifford ($d = 2$)	0.16 [26]	
$d = \infty$	1/2 [23]	1/2

To quantify the QEC capacity in the sub-thermal volume-law state ρ generated by the random quantum channel, we propose to study the mutual information $I_\rho(\{x\} : \bar{A}) = S^{(2)}_{\bar{\rho}}(\{x\}) + S^{(2)}_{\bar{\rho}}(\bar{A}) - S^{(2)}_{\bar{\rho}}(\{x\} \cup \bar{A})$ between a qudit at x (inside a region A) and the environment $\bar{A}$ (assuming $\bar{A}$ is larger than half of the system),

see Fig. 4(a). In terms of the entanglement feature state $|W_\rho\rangle$, we have (see Appendix F for derivation)

$$e^{I_\rho(\{x\}:\bar{A})} = \frac{\langle A|X_x|W_\rho\rangle\,\langle\Uparrow|W_\rho\rangle}{\langle A|W_\rho\rangle\,\langle\Uparrow|X_x|W_\rho\rangle}, \qquad (12)$$

where $|A\rangle = \prod_{i\in A} X_i\,|\Uparrow\rangle$ is the Ising basis state that specifies the region A. If $I_\rho(\{x\}:\bar{A})$ vanishes, measuring qudit x in A tells no information about $\bar{A}$, therefore the entanglement between A and $\bar{A}$ is unaffected by the measurement, suggesting that the information about $\bar{A}$ has been scrambled in region A to prevent local readout. It can be shown that the change of $S_\rho^{(2)}(A)$ after a measurement of strength p at a qudit at x distance away from the boundary of A is directly related to $I_\rho(\{x\}:\bar{A})$ in the weak measurement limit $p \to 0$ (see Appendix F),

$$\Delta S_x^{(2)}(A) \equiv -\log\frac{\langle A|\hat{T}_{M_x}|W_\rho\rangle}{\langle\Uparrow|\hat{T}_{M_x}|W_\rho\rangle} + \log\frac{\langle A|W_\rho\rangle}{\langle\Uparrow|W_\rho\rangle}$$
$$= -\frac{pd}{d+1}W_{\bar{\rho}}(\{x\})\big(e^{I_\rho(\{x\}:\bar{A})}-1\big) + \mathcal{O}(p^2), \qquad (13)$$

where $W_{\bar{\rho}}(\{x\})$ is the single-qudit purity (at position x). We found that the entropy drop depends on the measurement position x: a measurement deeper in the region A will be less effective in reducing the entropy of A. Our MPS-based numerical calculation in Fig. 4(b) confirms that $\Delta S_x^{(2)}(A) \sim -x^{-3/2}(|A|-x)^{-3/2}$ indeed follows the similar behavior as $I_\rho(\{x\}:\bar{A})$.[54] Both fall off with x in a power-law manner with the exponent 3/2. Given that the exponent 3/2 is greater than 1, the total entropy drop $\Delta S^{(2)}(A) = \sum_{x\in A} \Delta S_x^{(2)}(A)$ converges to a constant that does not scale with $|A|$, which can be balanced by the area-law entropy growth of the following unitary layer. Therefore the volume-law phase is stable. In Appendix G, we study the same problem in a certain random Clifford circuits and also observe the 3/2 exponent established above, which indicates the unversality of this result.

To develop analytical understanding of the exponent 3/2, we approximate the transfer matrices by $\hat{T}_{U_{ij}} \simeq e^{JZ_iZ_j}$ and $\hat{T}_{M_i} \simeq e^{hX_i}$. As $\hat{T}_{U_{ij}}$ ($\hat{T}_{M_i}$) can drive $|W_\rho\rangle$ towards the ferromagnetic (paramagnetic) state, the model still captures the volume-law (area-law) phase given $J > h$ ($J < h$). This simplification allows us to solve the leading eigenstate $|W_{\rho_\infty}\rangle$ of $\hat{T}_{\text{step}}$ analytically by mapping to the Majorana fermion basis $\chi_{2i-1} = \prod_{j<i} X_j Z_i$ and $\chi_{2i} = \prod_{j<i} X_j Y_i$ by Jordan-Wigner transformation. In the fermion language, the entanglement feature $W_{\rho_\infty}(A)$ of a single region A corresponds to a two-point strange correlator[55–57] between free fermion states (see Appendix H)

$$W_{\rho_\infty}(A) = \langle A|W_{\rho_\infty}\rangle = \langle\Uparrow|i\chi_0\chi_{2|A|+1}|W_{\rho_\infty}\rangle, \qquad (14)$$

which was originally introduced to diagnose symmetry protected topological (SPT) orders. If $|W_{\rho_\infty}\rangle$ is in the
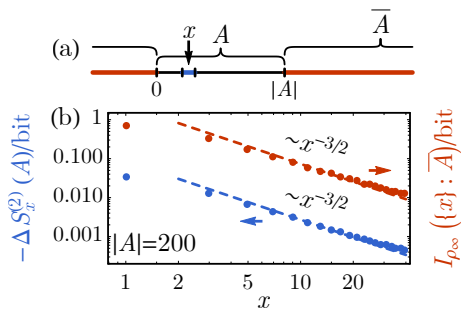

FIG. 4. (a) Entanglement region configuration for the mutual information $I_\rho(\{x\}:\bar{A})$. (b) Measurement-induced entropy drop $\Delta S_x^{(2)}(A)$ and the qubit-environment mutual information $I_{\rho_\infty}(\{x\}:\bar{A})$ for the final state of the random quantum channel (at $d=2, p=0.1$), based on the MPS of $|W_{\rho_\infty}\rangle$ with bond dimension 64.

topological (trivial) fermionic SPT phase (with respect to the reference state $|\Uparrow\rangle$)[58], the strange correlator $W_{\rho_\infty}(A)$ will exhibit a long-range correlation (an exponential decay) with respect to $|A|$, matching the area-law (volume-law) entropy scaling. We calculated the strange correlator deep in the trivial phase with $h \ll J$ (see Appendix H), and found

$$W_{\rho_\infty}(A) \propto \frac{e^{-\kappa|A|}}{|A|^{3/2}}, \qquad (15)$$

where $\kappa = \log(J/h)$. (The same power-law is derived in Ref. 59 from a different starting point based on the capillary-wave theory of entanglement domain walls.) This unveils an important entanglement feature of the sub-thermal volume-law steady state ρ_∞, namely the subleading logarithmic correction[26] of the single-region entanglement entropy $S_{\rho_\infty}^{(2)}(A) = \kappa|A| + \frac{3}{2}\log|A|$ with an universal coefficient 3/2. The free fermion representation of $|W_{\rho_\infty}\rangle$ enables us to evaluate multi-region entanglement features as multi-point strange correlators, which can then be decomposed to two-point strange correlators using Wick's theorem. For example, the factor $\langle A|X_x|W_{\rho_\infty}\rangle = -\langle\Uparrow|\chi_0\chi_{2x-1}\chi_{2x}\chi_{2|A|+1}|W_{\rho_\infty}\rangle$ on the numerator of Eq. (12) is a four-point correlator. Applying the asymptotic solution in Eq. (15), we can confirm that the measurement-induced entropy drop $\Delta S_x^{(2)}(A)$ indeed decays with the measurement position as $x^{-3/2}$ with the universal exponent 3/2, which is crucial to the stability of the volume-law phase. Finally, we show in Appendix E 2 that the sub-thermal volume-law state generated by Clifford unitary gates and random measurements indeed exhibits a power-law dependence of the entanglement drop with the measurement position, due to the power-law dependence of the stabilizer length distribution in the steady-state [26], though we are unable to analytically derive the precise exponent appearing in the power-law decay (for the case of Clifford rather than Haar random unitaries). Our discussion reveals the QEC

capacity of the sub-thermal volume-law state as a multi-region entanglement feature, which goes beyond the dichotomy of area-law v.s. volume-law scaling of the single-region entanglement entropy, and demonstrates the advantage of entanglement features in resolving finer structures of quantum many-body entanglement.

Order Parameter and Bulk Correlations— A natural question that arises is - how can we measure the $\mathbb{Z}_2$ Ising order parameter $\langle Z \rangle$ that appears within our mean-field description? In fact this is precisely the bulk order parameter identified in [29, 30], defined as the entanglement entropy of ancilla qudits, which are maximally entangled with the physical qudits during the circuit dynamics. The second Rényi entropy of a single ancilla is a function of the bulk magnetization $\langle Z \rangle$ and becomes proportional to it near the critical point and for $p > p_c$. Clearly in the strong measurement phase, the ancilla is decoupled from the physical qudits and the order parameter vanishes. Also, the second Rényi mutual information between two (space-time) separated ancillas is proportional to the connected bulk two point correlation $\langle Z_i Z_j \rangle_c$[29, 30] near the critial point. Although the mean-field theory is not expected to correctly capture the critical fluctuations, nevertheless by way of comparison we note that our Ising model mapping would imply, near the critical point, $\langle Z \rangle \propto (p_c - p)^\beta$ with $\beta = 1/8$ and $\langle Z_i Z_j \rangle_c = |i - j|^{-\eta}$ with $\eta = 1/4$, which, perhaps fortuitously, is close to the reported value in [29].

[1] A. Nahum, J. Ruhman, S. Vijay, and J. Haah, Quantum entanglement growth under random unitary dynamics, Phys. Rev. X **7**, 031016 (2017).

[2] T. Zhou and A. Nahum, Emergent statistical mechanics of entanglement in random unitary circuits, arXiv e-prints , arXiv:1804.09737 (2018), arXiv:1804.09737 [cond-mat.stat-mech].

[3] C. W. von Keyserlingk, T. Rakovszky, F. Pollmann, and S. L. Sondhi, Operator hydrodynamics, otocs, and entanglement growth in systems without conservation laws, Phys. Rev. X **8**, 021013 (2018).

[4] A. Nahum, S. Vijay, and J. Haah, Operator spreading in random unitary circuits, Phys. Rev. X **8**, 021014 (2018).

[5] A. Nahum, J. Ruhman, and D. A. Huse, Dynamics of entanglement and transport in one-dimensional systems with quenched randomness, Phys. Rev. B **98**, 035118 (2018).

[6] S. Vijay and A. Vishwanath, Finite-Temperature Scrambling of a Random Hamiltonian, arXiv.org (2018), 1803.08483.

[7] Y.-Z. You and Y. Gu, Entanglement features of random Hamiltonian dynamics, Phys. Rev. B **98**, 014309 (2018), arXiv:1803.10425 [quant-ph].

[8] T. Rakovszky, F. Pollmann, and C. W. von Keyserlingk, Diffusive hydrodynamics of out-of-time-ordered correlators with charge conservation, Phys. Rev. X **8**, 031058 (2018).

[9] A. Chan, A. De Luca, and J. T. Chalker, Spectral Statistics in Spatially Extended Chaotic Quantum Many-Body Systems, Phys. Rev. Lett. **121**, 060601 (2018), arXiv:1803.03841 [cond-mat.stat-mech].

[10] A. Chan, A. De Luca, and J. T. Chalker, Solution of a Minimal Model for Many-Body Quantum Chaos, Physical Review X **8**, 041019 (2018), arXiv:1712.06836 [cond-mat.stat-mech].

[11] B. Bertini, P. Kos, and T. Prosen, Entanglement Spreading in a Minimal Model of Maximal Many-Body Quantum Chaos, Physical Review X **9**, 021033 (2019), arXiv:1812.05090 [cond-mat.stat-mech].

[12] T. Rakovszky, C. W. von Keyserlingk, and F. Pollmann, Entanglement growth after inhomogenous quenches, arXiv e-prints , arXiv:1907.00869 (2019), arXiv:1907.00869 [cond-mat.str-el].

[13] N. Lashkari, D. Stanford, M. Hastings, T. Osborne, and P. Hayden, Towards the fast scrambling conjecture, Journal of High Energy Physics **2013**, 22 (2013), arXiv:1111.6580 [hep-th].

[14] P. Hosur, X.-L. Qi, D. A. Roberts, and B. Yoshida, Chaos in quantum channels, Journal of High Energy Physics **2016**, 4 (2016).

[15] D. N. Page, Average entropy of a subsystem, Phys. Rev. Lett. **71**, 1291 (1993).

[16] J. M. Deutsch, Quantum statistical mechanics in a closed system, Phys. Rev. A **43**, 2046 (1991).

[17] M. Srednicki, Chaos and quantum thermalization, Phys. Rev. E **50**, 888 (1994), arXiv:cond-mat/9403051 [cond-mat].

[18] M. Srednicki, Entropy and area, Phys. Rev. Lett. **71**, 666 (1993).

[19] F. Verstraete, M. M. Wolf, D. Perez-Garcia, and J. I. Cirac, Criticality, the Area Law, and the Computational Power of Projected Entangled Pair States, Physical Review Letters **96**, 220601 (2006), quant-ph/0601075.

[20] M. B. Hastings, An area law for one-dimensional quantum systems, Journal of Statistical Mechanics: Theory and Experiment **2008**, 24 (2008), arXiv:0705.2024 [quant-ph].

[21] Y. Li, X. Chen, and M. P. A. Fisher, Quantum Zeno effect and the many-body entanglement transition, Phys. Rev. B **98**, 205136 (2018), arXiv:1808.06134 [quant-ph].

[22] A. Chan, R. M. Nandkishore, M. Pretko, and G. Smith, Unitary-projective entanglement dynamics, Phys. Rev. B **99**, 224307 (2019), arXiv:1808.05949 [cond-mat.stat-mech].

[23] B. Skinner, J. Ruhman, and A. Nahum, Measurement-Induced Phase Transitions in the Dynamics of Entanglement, Physical Review X **9**, 031009 (2019),

arXiv:1808.05953 [cond-mat.stat-mech].

[24] Y. Bao, S. Choi, and E. Altman, Theory of the Phase Transition in Random Unitary Circuits with Measurements, arXiv e-prints , arXiv:1908.04305 (2019), arXiv:1908.04305 [cond-mat.stat-mech].

[25] C.-M. Jian, Y.-Z. You, R. Vasseur, and A. W. W. Ludwig, Measurement-induced criticality in random quantum circuits, arXiv e-prints , arXiv:1908.08051 (2019), arXiv:1908.08051 [cond-mat.stat-mech].

[26] Y. Li, X. Chen, and M. P. A. Fisher, Measurement-driven entanglement transition in hybrid quantum circuits, Phys. Rev. B **100**, 134306 (2019).

[27] S. Choi, Y. Bao, X.-L. Qi, and E. Altman, Quantum error correction and entanglement phase transition in random unitary circuits with projective measurements, arXiv e-prints , arXiv:1903.05124 (2019), arXiv:1903.05124 [quant-ph].

[28] M. J. Gullans and D. A. Huse, Dynamical purification phase transition induced by quantum measurements, arXiv e-prints , arXiv:1905.05195 (2019), arXiv:1905.05195 [quant-ph].

[29] A. Zabalo, M. J. Gullans, J. H. Wilson, S. Gopalakrishnan, D. A. Huse, and J. H. Pixley, Critical properties of the measurement-induced transition in random quantum circuits, arXiv e-prints , arXiv:1911.00008 (2019), arXiv:1911.00008 [cond-mat.dis-nn].

[30] M. J. Gullans and D. A. Huse, Scalable probes of measurement-induced criticality, (2019), arXiv:1910.00020 [cond-mat.stat-mech].

[31] M. Szyniszewski, A. Romito, and H. Schomerus, Entanglement transition from variable-strength weak measurements, arXiv e-prints , arXiv:1903.05452 (2019), arXiv:1903.05452 [cond-mat.stat-mech].

[32] Q. Tang and W. Zhu, Measurement-induced phase transition: A case study in the non-integrable model by density-matrix renormalization group calculations, arXiv e-prints , arXiv:1908.11253 (2019), arXiv:1908.11253 [cond-mat.stat-mech].

[33] R. Vasseur, A. C. Potter, Y.-Z. You, and A. W. W. Ludwig, Entanglement Transitions from Holographic Random Tensor Networks, arXiv e-prints , arXiv:1807.07082 (2018), arXiv:1807.07082 [cond-mat.stat-mech].

[34] W.-T. Kuo, A. A. Akhtar, D. P. Arovas, and Y.-Z. You, Markovian Entanglement Dynamics under Locally Scrambled Quantum Evolution, arXiv e-prints , arXiv:1910.11351 (2019), arXiv:1910.11351 [cond-mat.dis-nn].

[35] P. Hayden, S. Nezami, X.-L. Qi, N. Thomas, M. Walter, and Z. Yang, Holographic duality from random tensor networks, Journal of High Energy Physics **2016**, 9 (2016), arXiv:1601.01694 [hep-th].

[36] C. Jonay, D. A. Huse, and A. Nahum, Coarse-grained dynamics of operator and state entanglement, arXiv e-prints , arXiv:1803.00089 (2018), arXiv:1803.00089 [cond-mat.stat-mech].

[37] M. Mezei, Membrane theory of entanglement dynamics from holography, Phys. Rev. D **98**, 106025 (2018), arXiv:1803.10244 [hep-th].

[38] K. Kraus, A. Böhm, J. D. Dollard, and W. H. Wootters, *States, Effects, and Operations Fundamental Notions of Quantum Theory*, Vol. 190 (1983).

[39] T. A. Brun, A simple model of quantum trajectories, American Journal of Physics **70**, 719 (2002), arXiv:quant-ph/0108132 [quant-ph].

[40] For Clifford unitary dynamics with measurements in the Pauli basis, the entanglement properties of the state are independent of the measurement outcomes, so in this case, our protocol is actually identical to performing projective measurements.

[41] Y.-Z. You, Z. Yang, and X.-L. Qi, Machine learning spatial geometry from entanglement features, Phys. Rev. B **97**, 045153 (2018).

[42] J. Lopez-Piqueres and R. Vasseur, Mean-field theory of entanglement transitions from random tree tensor networks (2020), to appear.

[43] D. DiVincenzo, D. Leung, and B. Terhal, Quantum data hiding, IEEE Transactions on Information Theory **48**, 580 (2002).

[44] A. A. Akhtar and Y.-Z. You, Multi-Region Entanglement in Locally Scrambled Quantum Dynamics, arXiv e-prints , arXiv:2006.08797 (2020), arXiv:2006.08797 [cond-mat.dis-nn].

[45] F. Verstraete, V. Murg, and J. I. Cirac, Matrix product states, projected entangled pair states, and variational renormalization group methods for quantum spin systems, Advances in Physics **57**, 143 (2008), arXiv:0907.2796 [quant-ph].

[46] G. Vidal, Efficient simulation of one-dimensional quantum many-body systems, Phys. Rev. Lett. **93**, 040502 (2004).

[47] F. Verstraete, J. J. García-Ripoll, and J. I. Cirac, Matrix product density operators: Simulation of finite-temperature and dissipative systems, Phys. Rev. Lett. **93**, 207204 (2004).

[48] M. Zwolak and G. Vidal, Mixed-state dynamics in one-dimensional quantum lattice systems: A time-dependent superoperator renormalization algorithm, Phys. Rev. Lett. **93**, 207205 (2004).

[49] V. Zauner-Stauber, L. Vanderstraeten, M. T. Fishman, F. Verstraete, and J. Haegeman, Variational optimization algorithms for uniform matrix product states, Phys. Rev. B **97**, 045145 (2018), arXiv:1701.07035 [quant-ph].

[50] A. R. Calderbank and P. W. Shor, Good quantum error-correcting codes exist, Phys. Rev. A **54**, 1098 (1996), arXiv:quant-ph/9512032 [quant-ph].

[51] J. Preskill, Reliable quantum computers, Proceedings of the Royal Society of London Series A **454**, 385 (1998), arXiv:quant-ph/9705031 [quant-ph].

[52] This condition yields a so-called non-degenerate QEC code. A similar bound on degenerate quantum codes – were one to exist – may improve the bound on the critical measurement probability presented in Eq. (11).

[53] D. Gottesman, Class of quantum error-correcting codes saturating the quantum hamming bound, Phys. Rev. A **54**, 1862 (1996).

[54] The proportionality constant is also consistent with the corresponding single qudit purity which is computed separately.

[55] R. Shankar and A. Vishwanath, Equality of Bulk Wave Functions and Edge Correlations in Some Topological Superconductors: A Spacetime Derivation, Phys. Rev. Lett. **107**, 106803 (2011), arXiv:1105.5214 [cond-mat.str-el].

[56] Y.-Z. You, Z. Bi, A. Rasmussen, K. Slagle, and C. Xu, Wave Function and Strange Correlator of Short-Range Entangled States, Phys. Rev. Lett. **112**, 247202 (2014), arXiv:1312.0626 [cond-mat.str-el].

[57] K. Wierschem and K. S. D. Beach, Detection of symmetry-protected topological order in aklt states by

exact evaluation of the strange correlator, Phys. Rev. B **93**, 245141 (2016).

[58] Strictly speaking, the reference state should be $|\Uparrow\rangle + |\Downarrow\rangle$ to preserve fermion parity, but the entanglement feature remains the same, given the $\mathbb{Z}_2$ symmetry for pure states.

[59] Y. Li and M. P. A. Fisher, Statistical Mechanics of Quantum Error-Correcting Codes, arXiv e-prints , arXiv:2007.03822 (2020), arXiv:2007.03822 [quant-ph].

Appendix A: Numerical Validation of "Mean-Field" Approximation

In this appendix section, we will provide numerical evidence to support the "mean-field" approximation that enables us to evaluate the average entanglement entropy in the entanglement feature framework. We will first present simulation results of the random quantum channel model in finite-size systems, which demonstrate how measurement and average schemes affect the entanglement entropy calculation. We will then drill down further into the sample-to-sample fluctuation and reveal how its statistical properties ensure the validity of the "mean-field" approximation.

1. Measurement and Average Schemes

The "mean-field" approximation is central to this work, so we should carefully consider whether it is meaningfully accurate. To understand what we are comparing, we need to clarify: (a) what should be calculated as the commonly defined average entanglement entropy and (b) what is being calculated under the "mean-field" approximation. For this purpose, let us go through the simulation protocol, such that the measurement and average schemes can be described in a concrete context.

We start with a product state of N qudits (with on-site Hilbert space dimension d), say $|\Psi_0\rangle = |000\cdots0\rangle$. In the theoretical discussion, we will keep d general. But in the numerical simulation, we will always focus on the qubit case ($d = 2$). We simulate the evolution of the state vector $|\Psi\rangle$ starting from $|\Psi_0\rangle$. In each time step, we apply a unitary layer followed by a measurement layer as shown in Fig. 1. Note that here the definition of the time step is half of that in the main text. The purpose is to gain a finer resolution of time, to make better use of the data generated by the simulation. The unitary layer consists of two-site random unitary gates acting on even (odd) bonds for the even (odd) time step. Each gate is independently drawn from the Haar random ensemble. The state evolves as

$$|\Psi\rangle \to \prod_{\langle ij\rangle \in \text{even/odd}} U_{ij} |\Psi\rangle. \tag{A1}$$

In the measurement layer, each site will independently decide if a measurement should occur (with probability p) or not (with probability $1 - p$). If the measurement happens, it is implemented as a projective measurement (strong measurement) in the diagonal basis (Z basis). We define $P_{\alpha_i} = |\alpha\rangle_i \langle\alpha|_i$ to be the projection operator that projects the ith qudit to a particular basis state $|\alpha\rangle_i$ labeled by $\alpha = 0, \cdots, d - 1$. There are two options here regarding the *measurement scheme*:

- *Physical implementation.* In this scheme, we will follow the rule of quantum mechanics. If the measurement happens on a site i, we will first randomly pick a measurement outcome α_i according to the probability $p(\alpha_i) = \langle\Psi| P_{\alpha_i} |\Psi\rangle$, then the state $|\Psi\rangle$ will be projected and normalized

$$|\Psi\rangle \to \frac{P_{\alpha_i} |\Psi\rangle}{\sqrt{p(\alpha_i)}}. \tag{A2}$$

- *Projective implementation* (uniform random projectors). In this scheme, the measurement outcome α_i will be drawn with equal probability $p(\alpha_i) = 1/d$ regardless of the state $|\Psi\rangle$. Then the state $|\Psi\rangle$ will be updated as

$$|\Psi\rangle \to \sqrt{d} P_{\alpha_i} |\Psi\rangle. \tag{A3}$$

This is an unphysical process that does not even preserve the norm of the state. Nevertheless, it can still be simulated on a computer (we will not normalize $|\Psi\rangle$ in the simulation). This projective approach is also the underlying measurement scheme of the "mean-field" approximation, which effectively approximates the measurement probability $p(\alpha_i)$ by $1/d$ uniformly. It is somewhat reasonable because, after each unitary layer, the on-site basis has been fully scrambled, so there should not be any preference for any basis state on average, and all measurement outcomes should appear with equal probability. However, this is only an average statement, we must analyze the fluctuation on top of it more carefully, which will be presented below.

Following the above procedure, we can simulate the evolution of state $|\Psi\rangle$ for many random realizations of the random quantum channel model. Given an ensemble of quantum states $|\Psi\rangle$ (which might not be normalized) collected from the simulation at a particular time, we can evaluate the average entanglement entropy. We define $W_\Psi(A)$ to be the entanglement feature of $|\Psi\rangle$ in region A,

$$W_\Psi(A) = \text{Tr}_A(\text{Tr}_{\bar{A}} |\Psi\rangle \langle\Psi|)^2 = e^{-S_\Psi(A)}, \tag{A4}$$

regardless of whether $|\Psi\rangle$ is normalized or not. In terms of the entanglement feature $W_\Psi(A)$, we have two possible *average schemes*:

- *Arithmetic average* of entanglement feature $W_\Psi(A)$

$$\langle S\rangle(A) = -\ln \frac{\mathbb{E}_\Psi W_\Psi(A)}{\mathbb{E}_\Psi W_\Psi(\emptyset)} = -\ln \frac{\mathbb{E}_\Psi e^{-S_\Psi(A)}}{\mathbb{E}_\Psi e^{-S_\Psi(\emptyset)}}, \tag{A5}$$

where $\emptyset$ denotes the empty region and $\mathbb{E}_\Psi$ denotes the arithmetic average over states $|\Psi\rangle$ collected from simulation. Note that $S_\Psi(\emptyset)$ might not be zero since $|\Psi\rangle$ might not be normalized, such that the denominator could be non-trivial. The denominator provides the proper normalization for the arithmetic average of the entanglement feature. This is the average scheme taken in Eq. (7) for the "mean-field" approximation.

- *Geometric average* of entanglement feature $W_\Psi(A)$

$$\langle S\rangle(A) = -\mathbb{E}_\Psi \ln \frac{W_\Psi(A)}{W_\Psi(\emptyset)} = \mathbb{E}_\Psi S_\Psi(A) - \mathbb{E}_\Psi S_\Psi(\emptyset), \tag{A6}$$

which is also the arithmetic average of entanglement entropy $S_\Psi(A)$. This is the commonly used definition of the average 2nd Rényi entropy. The non-trivial "zero-point entropy" $\mathbb{E}_\Psi S_\Psi(\emptyset)$ is subtracted off in Eq. (A6), such that the formula applies to the case where the underlying quantum states $|\Psi\rangle$ are not normalized.

What we should calculate is the *physical measurements* with *geometric average* (phy+geo), but what is being calculated in the entanglement feature framework is the *random projectors* with *arithmetic average* (pro+ari). So the "mean-field" approximation contains two replacements: (1) replacing the physical measurement by the random projector and (2) replacing the geometric average by the arithmetic average. The goal here is to compare the resulting average entropy under these replacements in the numerical simulation. At this point, it will be natural to include the other two "intermediate" schemes (phy+ari) and (pro+geo) in the comparison as well, such that all together they complete the four possibilities of both measurement and average schemes. A full comparison could help to pin down the major source that leads to the deviation between the "mean-field" result and the actual result.

However, it is not very efficient to compare the average entanglement entropy in *all* possible entanglement regions. Because for a N-site system, there will be 2^N entanglement regions, such that a complete comparison would be unpractical. It turns out[44] that all the 2^N entanglement entropies form a dense continuum in Fig. 5 when $S(A)$ is collected by the region size $|A|$ (the same size $|A|$ can correspond to many possible regions A that cover the same number of sites but with different multi-region arrangements). We propose to focus on three representative entanglement regions: the single-site, the half-system, and the alternating-sites. They are representative regions in the sense that they are the anchor points that control the overall shape of the continuum. If we understand how these three cases are affected by different measurement and average schemes, we can pretty much infer similar behavior for the remaining multi-region entanglement entropies in the continuum.
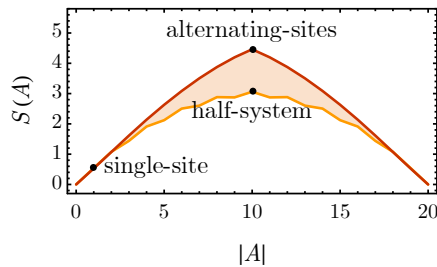

FIG. 5. The entanglement entropy continuum. The example is taken from a 20-site qubit system evolved by 30 steps with the measurement rate $p = 0.1$. The entanglement entropies are averaged over 100 samples.

2. Numerical Simulation and Scaling Analysis

We perform the numerical simulation of the random quantum channel model (keeping track of the pure state $|\Psi\rangle$ explicitly) with either the physical (phy) or the projective (pro) measurement scheme and calculate the evolution of the

single-site, half-system and alternating-sites entanglement entropies under either the geometric (geo) or the arithmetic (ari) average scheme. The simulation results are presented in Fig. 6, together with the result of the entanglement feature (EF) approach by evolving the entanglement feature state. On the overall level, different schemes look similar. They all capture the growth and the saturation of the entanglement entropy. The oscillatory behavior of the half-system entanglement entropy has to do with the fact that the entanglement region cuts through two immediate unitary gates in the even time step but not the odd time step. The pro+ari case shows the most significant fluctuation. But we can verify that the fluctuation is independent across different samples, such that all schemes have well-defined average in the large sample-size limit (as the relative error vanishes like $n^{-1/2}$ with the sample size $n \to \infty$ by the central limit theorem).
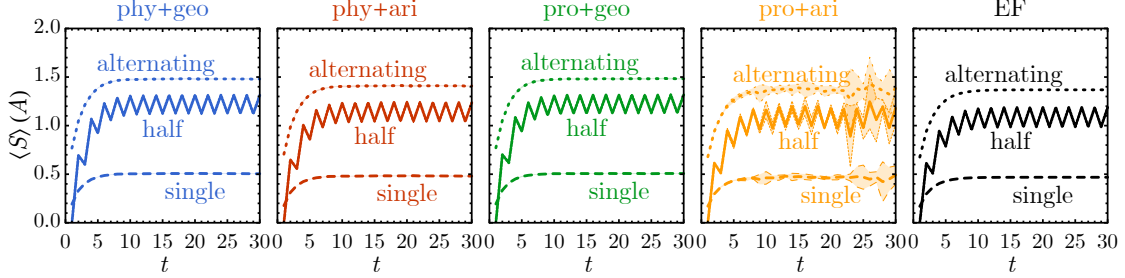

FIG. 6. Comparison between entanglement feature approach with numerical simulations under different schemes, showing how average entanglement entropies $\langle S \rangle (A)$ in three representative regions grow with time t. Simulation is done on a 8-site qubit system, evolved by 30 steps with the measurement rate $p = 0.1$. The entropy is averaged over 10000 samples in each batch. 5 batches are used to estimate the 2σ error margin, as indicated by the shaded band.
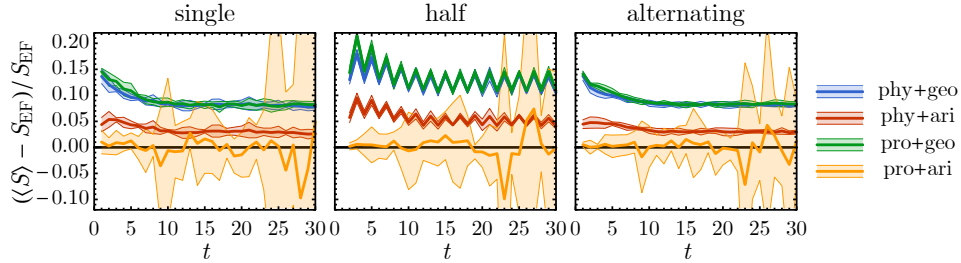

FIG. 7. The relative deviation of different measurement and average schemes from the entanglement feature approach. The simulation data is the same as Fig. 6. The shaded band indicates the 2σ error margin.

We should compare the phy+geo case (i.e. what should be calculated) with the pro+ari case (i.e. what converges to the EF approach). To zoom in the differences, we set the entanglement feature (EF) result $S_{\mathrm{EF}}(A)$ as a reference and subtract it from all the simulation results $\langle S \rangle (A)$ to obtain the *relative deviation* $(\langle S \rangle - S_{\mathrm{EF}})/S_{\mathrm{EF}}$, as shown in Fig. 7. Several observations can be drawn. Firstly, the pro+ari result fluctuates around the EF baseline and is expected to converge to the EF result in the large sample-size limit. We notice that for the half-system entanglement entropy, only the pro+ari result does not show the oscillatory behavior in the relative deviation, implying that there is no systematic deviation in this case, which is consistent with the fact that the EF approach is describing the large sample-size limit of the pro+ari scheme (see Ref. 34 for the theoretic proof of this fact). Secondly, all the other schemes have positive relative deviations, meaning that the EF approach always provides a lower bound for the average entropy (including phy+geo). Thirdly, it seems that the major gap between phy+geo and pro+ari is generated by switching from the geometric average to the arithmetic average. Changing the measurement scheme from the physical to projective implementation has a negligible effect under the geometric average (the underlying reason will be investigated in more detail later) and a minor effect under the arithmetic average. If we are allowed to redefine the average entanglement entropy by the arithmetic average of the entanglement feature, then the entanglement feature approach will provide a much tighter lower-bound. Finally, we can observe that the relative deviation does not grow with time and is stabilized to a level below 15% (for $p = 0.1$). The level of deviation is similar to the three representative choices of entanglement regions. Based on the intuition in Fig. 5 that these three points control the overall shape of the

multi-region entanglement entropy continuum, we expect all the 2^N entanglement entropies to exhibit a similar level of relative deviation.
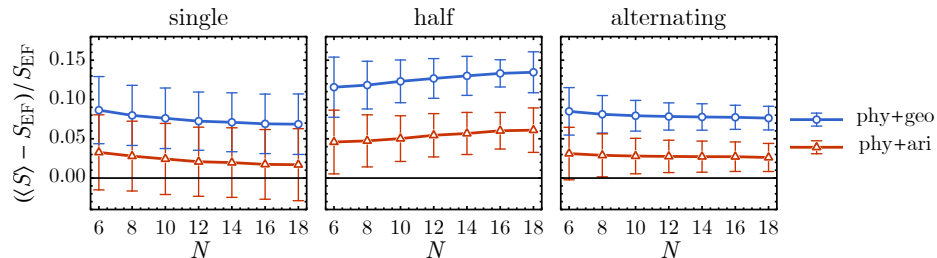

FIG. 8. Finite-size scaling of the relative deviation of the simulated entanglement entropy from the EF result. The simulation is done in qubit systems of different size N using the physical measurement scheme for 100 steps of evolution with measurement rate $p = 0.1$. The relative deviation is averaged over on 1000 samples in each batch through out the evolution. 10 batches are taken to estimate the error margin.

Then how does the deviation level scale with the system size? To answer this question, we perform a finite-size study of the relative deviation. As shown in Fig. 8, we do not observe a significant or systematic change beyond the error bar, as the system size enlarges from 6 to 18 by three times. The deviation level remains flat (within the error range) for all three representative entanglement regions. The conclusion is expected to hold for other entanglement regions as well. Combining results in Fig. 7 and Fig. 8, we conclude that the entanglement feature approach provides a lower bound for the average entanglement entropy with a stable relative gap, which does not seem the scale with both the evolution time and the system size. Thus we demonstrate the "tightness" of the lower bound and the validity of the "mean-field" approximation. Such relative deviation will affect quantitative measures such as the volume law coefficient. But we expect that the scaling behaviors are not affected, such as how the measurement-induced entropy drop $\Delta S_x(A) \sim x^{-3/2}$ scales with the measurement position x (which we studied in this work).
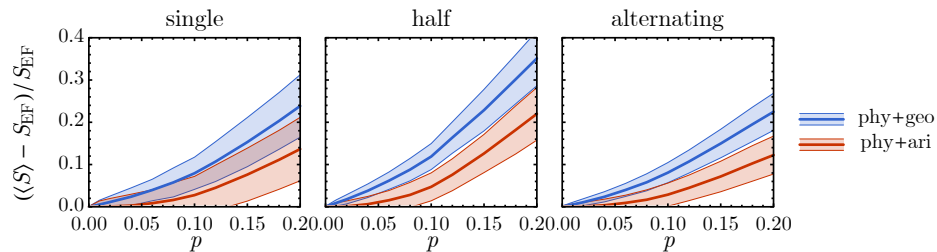

FIG. 9. The dependence of the relative deviation on the measurement rate. Data taken from simulations on 8-site qubit systems over 100 steps of evolution at different measurement rates. The relative deviation is averaged over on 1000 samples in each batch through out the evolution. 10 batches are taken to estimate the error margin.

Finally, the relative deviation of entanglement entropy is expected to increase with the measurement rate significantly. We show the measurement rate dependence in Fig. 9. In the $p \to 0$ limit, when there is no measurement, the deviation between phy+ari and pro+ari (which is the EF baseline) should vanish exactly, as the measurement scheme no longer matters. This is confirmed in Fig. 9 (red curves) for all choices of entanglement regions. However, phy+geo (blue curves) still has a finite deviation, since the two average schemes are still going to make a difference as long as there are sample-to-sample fluctuations. It turns out that the deviation is very small in the $p \to 0$ limit. As the measurement rate p increases, the deviations for both phy+geo and phy+ari grow rapidly. Therefore the "mean-field" approximation and the entanglement feature approach might only apply to the volume-law phase when the measurement rate p is small. But the approximation will fail for larger p near the entanglement transition or beyond.

3. Fluctuation Statistics under Extensive Measurements

Here we further investigate the essential statistical properties in the sample-to-sample fluctuation of the entanglement entropy and the state normalization factor that underlies the "mean-field" approximation. The main assumption in the approximation is that the fluctuation of the trace of the unnormalized density matrix $\mathrm{Tr}\,\rho$ is uncorrelated with the fluctuation of the unnormalized entanglement feature $\mathrm{Tr}\,\rho^{\otimes 2}\mathcal{X}_\sigma$, such that their averages can be evaluated separately on the numerator and the denominator in Eq. (7). To properly check this approximation, we need to consider the statistics of an extensive number of measurements on the system, because the variance can accumulate over time (and space) as more measurements are made.

To understand this issue in further details, we step back and revisit the simulation data under the *physical* measurement scheme, where the state norm is preserved at unity. We can collect the probability $p(\alpha_I)$ associated with each measurement outcome α_I in the evolution history, where $I = (i, t)$ labels the measurement instance in the spacetime (at site i and time t). We multiply these probabilities together to define the *outcome probability* associated with the final state $|\Psi\rangle$,

$$p_\Psi = \prod_I p(\alpha_I) = \mathrm{Tr}(E[P, U]\rho_0 E[P, U]^\dagger), \tag{A7}$$

which is the probability for a particular final state $|\Psi\rangle$ to occur condition on the realization of all unitary gates and the assignment of all measurement positions (but not the measurement outcomes). It can be rewritten in Eq. (A7) in terms of the initial state $\rho_0 = |\Psi_0\rangle\langle\Psi_0|$ and the *time-ordered* product $E[P, U]$ of all the projection and unitary operators involved in the history:

$$E[P, U] = \mathcal{T}\prod_{I, J} P_{\alpha_I} U_J. \tag{A8}$$

We expect p_Ψ to decay with time exponentially: as more measurements are performed, the probability that we get a particular final state will become smaller. This expectation is verified in our simulation, as exemplified in Fig. 10(a). We find that $\log_d p_\Psi$ closely follows the negative number of measurements, i.e. $\log_d p_\Psi \simeq -m_\Psi$, where $m_\Psi = \sum_I 1$ counts the number of measurements that has been performed to obtain the state $|\Psi\rangle$. This is consistent with the intuition that each measurement roughly contributes a $1/d$ factor to the outcome probability, such that $p_\Psi \sim d^{-m_\Psi}$. This observation motivates the "mean-field" approximation to replace the physical measurement by random projectors with fixed $1/d$ outcome probability. However, we must analyze how $\log_d p_\Psi$ fluctuates around $-m_\Psi$ more carefully, as the deviation may accumulate in time.
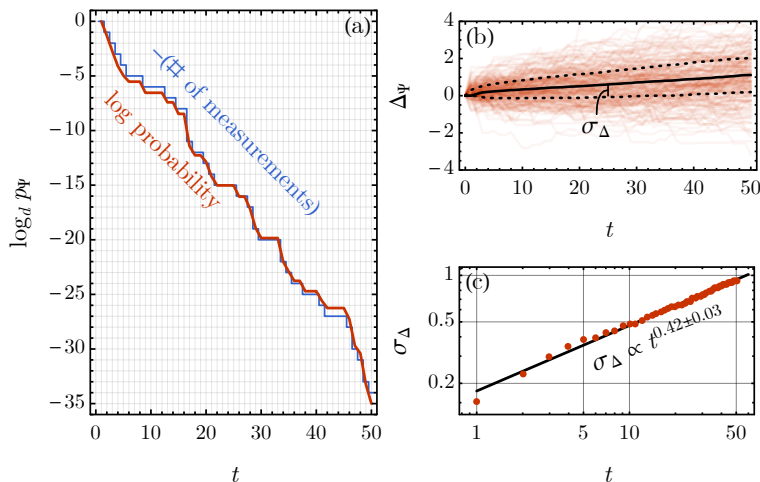

FIG. 10. (a) An example of outcome probability p_Ψ (in log scale) as a function of time t, plotted on top of the negative number of measurements. The example is taken from a 8-site qubit system for 50 steps of evolution with the measurement rate $p = 0.1$. (b) Examples of the gap Δ_Ψ fluctuating with time t. The solid line is the mean of Δ_Ψ. The dashed lines are the 1σ deviation of Δ_Ψ. The statistics are collected over 5000 samples. (c) The time dependence of the gap fluctuation σ_Δ in double-log plot.

To this purpose, we define the deviation in the log scale as

$$\Delta_\Psi = \ln \frac{p_\Psi}{d^{-m_\Psi}} = \ln p_\Psi + m_\Psi \ln d, \tag{A9}$$

and call it a "gap". In Fig. 10(b), we show how the gap Δ_Ψ drifts and diffuses with time. The drift can be understood because as p_Ψ fluctuates around d^{-m_Ψ} there is a preference to sample $|\Psi\rangle$ with an outcome probability greater than average. This bias will accumulate in time, leading to the drift of the average gap $\langle\Delta\rangle$ in a positive direction. Moreover, we also observe that the fluctuation of Δ_Ψ also broadens in time. The standard deviation σ_Δ exhibits a power-law scaling with time in Fig. 10(c). The power deviates from $1/2$, indicating a non-trivial autocorrelation in time, but we will not further analyze it as it is not essential to our discussion. In conclusion, the deviation between p_Ψ and d^{-m_Ψ} does grow in time (also in system size) as Δ_Ψ diffuses, but it does not necessarily mean that the "mean-field" approximation is getting worse with time (or system size). The "mean-field" approach is not simply about replacing the measurement outcome probability $p(\alpha_I)$ by the uniform $1/d$ probability. Its validity relies on how the fluctuation of Δ_Ψ is correlated with the fluctuation of entanglement entropy S_Ψ across samples.

We take a closer look at what happens when we switch the measurement scheme from physical to projective (e.g. from phy+geo to pro+geo). Let $\mathcal{E}_{\text{phy}} = \{|\Psi\rangle\}$ be an ensemble of states collected from simulation with the physical measurement scheme (such that $|\Psi\rangle$ is normalized). According to Eq. (A2), the final sate $|\Psi\rangle$ is related to the initial state $|\Psi_0\rangle$ by

$$|\Psi\rangle = \frac{E[P,U]\,|\Psi_0\rangle}{\sqrt{\prod_I p(\alpha_I)}} = \frac{1}{\sqrt{p_\Psi}} E[P,U]\,|\Psi_0\rangle, \tag{A10}$$

where $E[P,U]$ was defined in Eq. (A8). For each state $|\Psi\rangle$, define the entanglement entropy $S_\Psi(A)$ by Eq. (A4). As $|\Psi\rangle$ is normalized, the "zero-point" entropy $S_\Psi(\emptyset) = 0$ vanishes. Let us first consider the geometric average of entanglement features (i.e. arithmetic average of entanglement entropies), where the average entropy follows from Eq. (A6)

$$\langle S\rangle_{\text{phy}}(A) = \mathbb{E}_\Psi S_\Psi(A) - \mathbb{E}_\Psi S_\Psi(\emptyset) = \frac{1}{|\mathcal{E}_{\text{phy}}|} \sum_{\Psi \in \mathcal{E}_{\text{phy}}} S_\Psi(A), \tag{A11}$$

where $|\mathcal{E}_{\text{phy}}|$ denotes the number of samples in $\mathcal{E}_{\text{phy}}$. Now if we switch to the random projector implementation, there will be two modifications to Eq. (A11):

- The resulting sate $|\Psi'\rangle$ is no longer normalized. According to Eq. (A3), the unnormalized state is given by

$$|\Psi'\rangle = \left(\prod_I \sqrt{d}\right) E[P,U]\,|\Psi_0\rangle = \sqrt{d^{m_\Psi}} E[P,U]\,|\Psi_0\rangle. \tag{A12}$$

  Comparing with Eq. (A10), $|\Psi'\rangle$ and $|\Psi\rangle$ differ by a factor: $|\Psi'\rangle = \sqrt{d^{m_\Psi} p_\Psi}\,|\Psi\rangle = e^{\Delta_\Psi/2}\,|\Psi\rangle$. By definition in Eq. (A4), the factor $e^{\Delta_\Psi/2}$ will shift the entanglement entropy by $-2\Delta_\Psi$, such that

$$S_{\Psi'}(A) = S_\Psi(A) - 2\Delta_\Psi. \tag{A13}$$

- The outcome probability for the state $|\Psi'\rangle$ to occur is deformed, such that the state drawn from $\mathcal{E}_{\text{phy}}$ should be reweighted by d^{-m_Ψ}/p_Ψ to match the statistical distribution of $\mathcal{E}_{\text{pro}}$. Such as

$$\frac{1}{|\mathcal{E}_{\text{pro}}|} \sum_{\Psi' \in \mathcal{E}_{\text{pro}}} S_{\Psi'}(A) = \frac{1}{Z} \sum_{\Psi \in \mathcal{E}_{\text{phy}}} \frac{d^{-m_\Psi}}{p_\Psi} S_{\Psi'}(A) = \frac{1}{Z} \sum_{\Psi \in \mathcal{E}_{\text{phy}}} (S_\Psi(A) - 2\Delta_\Psi)e^{-\Delta_\Psi}, \tag{A14}$$

  where the partition function is $Z = \sum_{\Psi \in \mathcal{E}_{\text{phy}}} e^{-\Delta_\Psi}$.

Given these, the average entropy becomes

$$\begin{aligned}
\langle S\rangle_{\text{pro}}(A) &= \mathbb{E}_\Psi S_\Psi(A) - \mathbb{E}_\Psi S_\Psi(\emptyset) = \frac{1}{|\mathcal{E}_{\text{pro}}|} \sum_{\Psi' \in \mathcal{E}_{\text{pro}}} S_{\Psi'}(A) - \frac{1}{|\mathcal{E}_{\text{pro}}|} \sum_{\Psi' \in \mathcal{E}_{\text{pro}}} S_{\Psi'}(\emptyset) \\
&= \frac{1}{Z} \sum_{\Psi \in \mathcal{E}_{\text{phy}}} (S_\Psi(A) - 2\Delta_\Psi)e^{-\Delta_\Psi} - \frac{1}{Z} \sum_{\Psi \in \mathcal{E}_{\text{phy}}} (-2\Delta_\Psi)e^{-\Delta_\Psi} \\
&= \frac{1}{Z} \sum_{\Psi \in \mathcal{E}_{\text{phy}}} S_\Psi(A)e^{-\Delta_\Psi}.
\end{aligned} \tag{A15}$$

Eq. (A15) enables us to calculate the average entanglement entropy for the projective measurement scheme by reweighting the samples from the physical measurement scheme, which forms the basis for us to compare $\langle S \rangle_{\mathrm{pro}}$ and $\langle S \rangle_{\mathrm{phy}}$. It becomes clear that Δ_Ψ serves as an action that deforms the expectation value of S_Ψ. To the leading order in Δ_Ψ, the deviation is given by the correlation between Δ_Ψ and S_Ψ evaluated on samples in $\mathcal{E}_{\mathrm{phy}}$,

$$
\begin{aligned}
\langle S \rangle_{\mathrm{pro}} &= \frac{\sum_{\Psi \in \mathcal{E}_{\mathrm{phy}}} S_\Psi e^{-\Delta_\Psi}}{\sum_{\Psi \in \mathcal{E}_{\mathrm{phy}}} e^{-\Delta_\Psi}} \\
&= \frac{\sum_{\Psi \in \mathcal{E}_{\mathrm{phy}}} S_\Psi (1 - \Delta_\Psi)}{\sum_{\Psi \in \mathcal{E}_{\mathrm{phy}}} (1 - \Delta_\Psi)} + \mathcal{O}(\Delta_\Psi^2) \\
&= \frac{\langle S \rangle_{\mathrm{phy}} - \langle S\Delta \rangle_{\mathrm{phy}}}{1 - \langle \Delta \rangle_{\mathrm{phy}}} + \mathcal{O}(\Delta_\Psi^2) \\
&= \langle S \rangle_{\mathrm{phy}} - (\langle S\Delta \rangle_{\mathrm{phy}} - \langle S \rangle_{\mathrm{phy}} \langle \Delta \rangle_{\mathrm{phy}}) + \mathcal{O}(\Delta_\Psi^2).
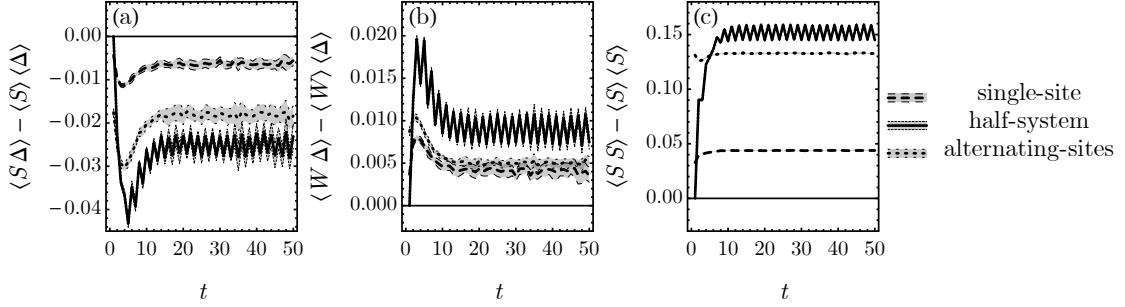\end{aligned}
\tag{A16}
$$

FIG. 11. Correlation on samples collected in the simulation with physical measurement scheme. The simulation is done on a 8-site qubit system for 50 steps of evolution with the measurement rate $p = 0.1$. Correlation is analyzed over 50000 samples in each batch. 4 batches are taken to estimate the error margin.

Despite of the steady growth of the gap fluctuation $\langle \Delta^2 \rangle_{\mathrm{phy}} - \langle \Delta \rangle_{\mathrm{phy}}^2$ as shown in Fig. 10, the entropy-gap correlation $\langle S\Delta \rangle_{\mathrm{phy}} - \langle S \rangle_{\mathrm{phy}} \langle \Delta \rangle_{\mathrm{phy}}$ remains small and stable in time as shown in Fig. 11(a) for all representative entanglement regions. This is a key statistical feature that controls the proximity between $\langle S \rangle_{\mathrm{pro}}$ and $\langle S \rangle_{\mathrm{phy}}$. The fact that the correlation is negative also explains why $\langle S \rangle_{\mathrm{pro}}$ is slightly larger than $\langle S \rangle_{\mathrm{phy}}$, as observed in Fig. 7 (by comparing pro+geo and phy+geo). Although the perturbative analysis in Eq. (A16) does not immediately tell that all the higher order terms in Δ_Ψ are controlled in a similar manner, nevertheless, the non-perturbative numerical simulation result in Fig. 7 has already lend support to the convergence of the higher order terms. In conclusion, our analysis of the sample-to-sample fluctuation under extensive measurements reveals the small entropy-gap correlation, which enables the replacement of the physical measurement by random projectors and sets the basis for the "mean-field" approximation.

Now we consider the other average scheme, i.e. the arithmetic average of entanglement features. Following the same procedure, we can analyze the average entanglement feature under different measurement schemes. Starting from Eq. (A5), we have

$$
\begin{aligned}
\langle W \rangle_{\mathrm{phy}}(A) &= \frac{1}{|\mathcal{E}_{\mathrm{phy}}|} \sum_{\Psi \in \mathcal{E}_{\mathrm{phy}}} W_\Psi(A), \\
\langle W \rangle_{\mathrm{pro}}(A) &= \frac{1}{Z} \sum_{\Psi \in \mathcal{E}_{\mathrm{phy}}} W_\Psi(A) e^{\Delta_\Psi}.
\end{aligned}
\tag{A17}
$$

The partition function here should be $Z = \sum_{\Psi \in \mathcal{E}_{\mathrm{phy}}} e^{\Delta_\Psi}$, such that $\langle W \rangle_{\mathrm{pro}}(\emptyset) = 1$. To the leading order in Δ_Ψ, the deviation between these two averages is given by the correlation between Δ_Ψ and W_Ψ,

$$
\langle W \rangle_{\mathrm{pro}} = \langle W \rangle_{\mathrm{phy}} + (\langle W\Delta \rangle_{\mathrm{phy}} - \langle W \rangle_{\mathrm{phy}} \langle \Delta \rangle_{\mathrm{phy}}) + \mathcal{O}(\Delta_\Psi^2).
\tag{A18}
$$

As we show in Fig. 11(b), the correlation is also stable in time, which controls the proximity between $\langle W \rangle_{\mathrm{pro}}$ and $\langle W \rangle_{\mathrm{phy}}$. The positive correlation is also consistent with the fact that $-\ln\langle W \rangle_{\mathrm{pro}}$ will be smaller than $-\langle W \rangle_{\mathrm{phy}}$, as observed in Fig. 7 (by comparing pro+ari and phy+ari).

Finally, we can compare the two average schemes. We have

$$-\ln\langle W \rangle = \langle S \rangle - \frac{1}{2}(\langle S^2 \rangle - \langle S \rangle^2) + \mathcal{O}(S_\Psi^3). \tag{A19}$$

On the left-hand-size, $-\ln\langle W \rangle$ is the entanglement entropy from the arithmetic average of the entanglement feature. On the right-hand-size, $\langle S \rangle$ is the entanglement entropy from the geometric average of the entanglement feature. Their difference is given by the variance of the entanglement entropy to the leading order. We show in Fig. 11(c) that the entropy fluctuation is also stable in time.

In conclusion, we numerically check the various correlations in Fig. 11 under extensive measurements over a long time. We observe that these correlations do not grow with the number of measurements as time evolves, which supports that the deviations between different measurement and average schemes will remain stable. We expect the correlations to exhibit the same stability under system-size scaling as well because the major effect of enlarging the system size is also to increase the number of measurements. Combining these analyses, we demonstrate the essential statistical features in the sample-to-sample fluctuation that justify our "mean-field" approximation.

Appendix B: Check for the Ising universality

In this section, we check the critical point in our "mean-field" model falls into the Ising universality class.

As shown in Fig. 2, the volume-law coefficient has a discontinuity at a certain critical value of p_c, which exhibits a phase transition. To verify that systems with different qudit dimensions d share the same universality class of the transition, let us rescale the data and plot $f \log d$ as a function of $p_c - p$ for $p < p_c$ and results are in Fig. 12. Different curves collapsing with each other implies that they can be captured by the same scaling function $F((p_c - p)^\nu L)$. A further fitting yields that the critical exponent is $\nu = 1$, which implies that the entanglement transition falls into the Ising universality class under the mean-field description. Although the actual universality class of the entanglement transition is beyond Ising, the result here is still meaningful in verifying that the entanglement dynamics can be approximated by a imaginary time Floquet problem of Ising model, see Eq. (H1).
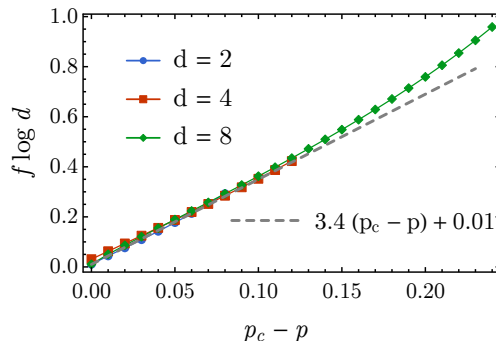

FIG. 12. The volume-law coefficients with respect to the measurement probability for different qudit dimension. The horizontal axis is $p_c - p$ and the vertical axis is $f \log d$, for which p_c and $\log d$ are chosen for different qudits respectively. All colored curves collapses for p close to p_c. The gray curve is a linear function, which implies the critical exponent is $\nu = 1$.

Appendix C: Entanglement Feature Operators

To construct the transfer matrix $\hat{T}_K$ of a Kraus operator K, we need to first calculate the corresponding entanglement feature operator $\hat{W}_K$. We direct the reader to Ref. 34, where the entanglement feature operator for the identity operator $\hat{W}_\mathbb{I}$ and the two-qudit Haar random unitary gate $\hat{W}_{U_{ij}}$ has been calculated. The result is

$$\hat{W}_\mathbb{I} = \prod_i d(d + X_i),$$
$$\hat{W}_{U_{ij}} = d^2(d + X_i)(d + X_j) - \frac{d^2(d^2 - 1)}{2(d^2 + 1)}(1 - Z_i Z_j)(d^2 - X_i X_j). \tag{C1}$$

With these, we can already construct the transfer matrix for the unitary gate as

$$\hat{T}_{U_{ij}} = \hat{W}_{U_{ij}} \hat{W}_{\mathbb{I}}^{-1} = \left(1 + \frac{d}{d^2+1}(X_i + X_j)\right)\frac{1 + Z_i Z_j}{2}. \tag{C2}$$

Here we derive the entanglement feature operator for the single-qudit measurement M, drawn from the ensemble $\mathcal{E}_M = \{\mathbb{I}\} \cup \{\sqrt{d}P_V | V \in U(d)\}$ (where $P_V = V |0\rangle \langle 0| V^\dagger$), equipped with the probability measure $P(\mathbb{I}) = 1 - p$ and $P(\sqrt{d}P_V) = p\,dV$. By definition

$$\begin{aligned}
W_M[\sigma, \tau] &= \mathbb{E}_{M \in \mathcal{E}_M} \operatorname{Tr} M^{\dagger \otimes 2} \mathcal{X}_\sigma M^{\otimes 2} \mathcal{X}_\tau \\
&= (1-p) \operatorname{Tr} \mathbb{I}^{\dagger \otimes 2} \mathcal{X}_\sigma \mathbb{I}^{\otimes 2} \mathcal{X}_\tau + pd^2 \int_{U(d)} dV \operatorname{Tr} P_V^{\dagger \otimes 2} \mathcal{X}_\sigma P_V^{\otimes 2} \mathcal{X}_\tau \\
&= (1-p) \operatorname{Tr} \mathcal{X}_\sigma \mathcal{X}_\tau + pd^2 \int_{U(d)} dV \operatorname{Tr}(|0\rangle \langle 0|)^{\otimes 2} \mathcal{X}_\sigma (|0\rangle \langle 0|)^{\otimes 2} \mathcal{X}_\tau \\
&= (1-p)d^{\frac{3+\sigma\tau}{2}} + pd^2.
\end{aligned} \tag{C3}$$

In terms of the operator form, we have

$$\hat{W}_M = \sum_{[\sigma, \tau]} |\sigma\rangle W_M[\sigma, \tau] \langle \tau| = d^2 + ((1-p)d + pd^2)X, \tag{C4}$$

from which the transfer matrix $\hat{T}_M$ can be constructed,

$$\hat{T}_{M_i} = \hat{W}_{M_i} \hat{W}_{\mathbb{I}}^{-1} = 1 - \frac{p}{d+1} + \frac{dp}{d+1}X_i, \tag{C5}$$

where we have attached the site index i. Putting together Eq. (C2) and Eq. (C5), we obtain the transfer matrices given in Eq. (8). The transfer matrix for each layer of the quantum channel can be further constructed out of these basic transfer matrices.

Appendix D: Matrix Product State and Numerical Approaches

1. MPS Representation of Entanglement Feature State

The entanglement feature state $|W_\rho\rangle$ was introduced to encode the entanglement feature of a many-body state ρ. But $|W_\rho\rangle$ itself is also a many-body state of Ising spins. We can further ask what is the entanglement property of $|W_\rho\rangle$? Is it an area-law state or a volume-law state? We do not have a full answer for this question in general, but the current understanding is that even the underlying physical state ρ is volume-law entangled, its entanglement feature state $|W_\rho\rangle$ can still be area-law entangled. This can be shown by an explicit construction of the matrix product state (MPS) representation for the entanglement feature state of the Page state (which is an extreme limit of the volume-law state with maximal thermalization). Let us consider the following translational invariant MPS ansatz for the entanglement feature

$$W_\rho[\sigma] = \operatorname{Tr}(\cdots A^{\sigma_{i-1}} A^{\sigma_i} A^{\sigma_{i+1}} \cdots), \tag{D1}$$

where A^σ is a matrix specified by the Ising spin $\sigma = \pm 1$. We claim that the following setting of A^σ gives an exact MPS representation (up to a normalization constant) for the entanglement feature of the Page state

$$A^\sigma = \begin{bmatrix} d^{\sigma/2} & 0 \\ 0 & d^{-\sigma/2} \end{bmatrix}. \tag{D2}$$
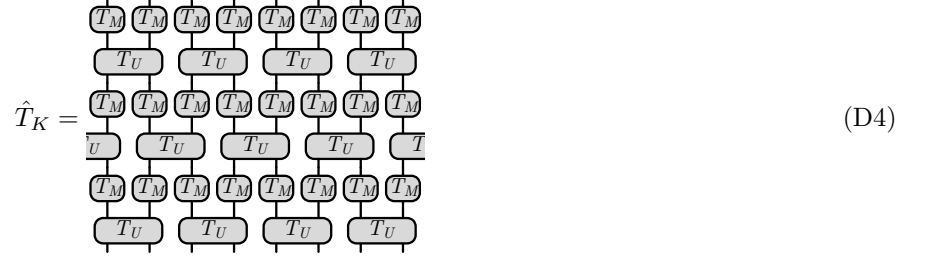
Plugging Eq. (D2) to Eq. (D1), we can show

$$\begin{aligned}
W_\rho[\sigma] &= \operatorname{Tr} \prod_i \begin{bmatrix} d^{\sigma_i/2} & 0 \\ 0 & d^{-\sigma_i/2} \end{bmatrix} = d^{\frac{1}{2}\sum_i \sigma_i} + d^{-\frac{1}{2}\sum_i \sigma_i}, \\
S_{\tilde{\rho}}^{(2)}[\sigma] &= -\log \frac{W_\rho[\sigma]}{W_\rho[\Uparrow]} = -\log \frac{d^{\frac{1}{2}\sum_i \sigma_i} + d^{-\frac{1}{2}\sum_i \sigma_i}}{d^{\frac{N}{2}} + d^{-\frac{N}{2}}}.
\end{aligned} \tag{D3}$$

This precisely matches the entanglement feature of the Page state for N qudits (each of the dimension d). It produces the volume-law entanglement entropy scaling with maximal volume-law coefficient $f = 1$. So the Page state entanglement feature admits an MPS representation of bond dimension 2. On the other hand, the product state entanglement feature $W_\rho[\sigma] = 1$ can obviously be produced by an even simpler ansatz $A^\sigma = \begin{bmatrix} 1 \end{bmatrix}$, which is of the bond dimension 1. We can see, both the unentangled and maximally-entangled limit of the entanglement feature can be captured by MPS with low bond dimension. It is conceivable that the MPS ansatz may provide pretty good description for intermediate states across the entanglement transition as well. It is also expected that the MPS description will fall short at the transition: as $|W_\rho\rangle$ becomes critical, the required MPS bond dimension scales with the system size logarithmically.

We use two MPS-based numerical approaches in this work: the time-evolving block decimation (TEBD) algorithm[46–48] and the variational uniform matrix product state (VUMPS) algorithm[49]. We use the TEBD algorithm to evolve the entanglement feature state $|W_\rho\rangle$ in time following entanglement dynamics specified by the random quantum channel model. We use the VUMPS to find the final entanglement feature state $|W_{\rho_\infty}\rangle$ in the long-time limit (as the leading eigenstate of the transfer matrix).

2. TEBD Approach

We first introduce the TEBD approach. We study the entanglement dynamics under the random quantum channel model. The evolution of the entanglement feature state $|W_\rho\rangle \to \hat{T}_K |W_\rho\rangle$ is governed by the transfer matrix $\hat{T}_K$ of the quantum channel K,

$$\hat{T}_K = \quad\text{(D4)}$$

which consists of the transfer matrix $\hat{T}_{U_{ij}}$ for the two-qudit unitary gate U_{ij} and the transfer matrix $\hat{T}_{M_i}$ for the single-qudit weak measurement M_i. They are arranged in the brick-wall pattern as shown in Eq. (D4). Their expressions are given in Eq. (C2) and Eq. (C5) respectively. We start with the entanglement feature state of product states $|W_\rho\rangle = \sum_{[\sigma]} |\sigma\rangle$, which is translation invariant. Because the transfer matrix has a 2-site translation symmetry, we expect that the resulting entanglement feature state will also respect the 2-site translation symmetry, and can be described by an MPS ansatz with 2-site unit-cells,

$$W_\rho[\sigma] = \text{Tr}\left(\prod_j A_1^{\sigma_{2j-1}} A_2^{\sigma_{2j}} \right) = \text{Tr}(\cdots \text{—} A_1 \text{—} A_2 \text{—} A_1 \text{—} A_2 \text{—} \cdots). \quad\text{(D5)}$$

The MPS tensors are initialized to

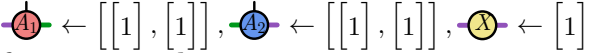$$A_1^\sigma = A_2^\sigma = \begin{bmatrix} 1 \end{bmatrix}, \quad\text{(D6)}$$

which parameterizes the entanglement feature of product states. We then apply the TEBD algorithm, as described in Algorithm 1, to evolve the MPS representation of $|W_\rho\rangle$ in time, where transfer matrices $\hat{T}_U$ and $\hat{T}_M$ are applied to $|W_\rho\rangle$ step-by-step following Eq. (D4).

Algorithm 1 Applying TEBD to evolve the MPS of $|W_\rho\rangle$

---

input: $\hat{T}_U = \boxed{T_U}$, $\hat{T}_M = \boxed{T_M}$ - transfer matrices of two-qudit gate $\hat{T}_U$ and single-qudit measurement $\hat{T}_M$.

output: $|W_\rho\rangle = \text{Tr}(\cdots \text{—} A_1 \text{—} A_2 \text{—} A_1 \text{—} A_2 \text{—} \cdots)$ - MPS representation of the entanglement feature state after T steps of evolution (following the brick-wall circuit).

1: **procedure** TEBD(T)

2: $\leftarrow \left[[1],[1]\right]$, $\leftarrow \left[[1],[1]\right]$, $\leftarrow [1]$ ▷ initialization (start with $|W_\rho\rangle$ of product states)

3:     **for** $t = 1 : 2T$ **do**   ▷ evolves for T steps

4:        (, ,) $\leftarrow$ TEBD.iterate(, ,)
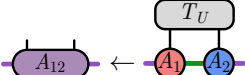
5:     **end for**

6:     **return** (,)

7: **end procedure**

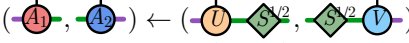8: **function** TEBD.iterate(A_1, A_2, X)
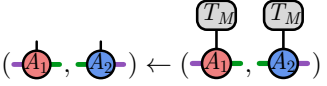
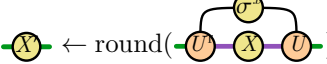9:   (, ,) $\leftarrow (A_1, A_2, X)$ ▷ import MPS tensors A_1, A_2 and symmetry operator X

10:      $\leftarrow$ ▷ apply transfer matrix $\hat{T}_U$
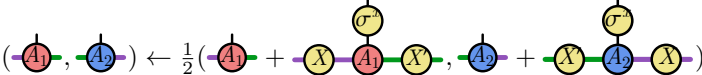
11:      $\leftarrow$ SVD(, up to D_{cut})   ▷ perform SVD up to cutoff dimension D_{cut}

12:      $\leftarrow$ sqrt(/max( ))   ▷ normalize singular values and take square root

13:     (,) $\leftarrow$ (,)   ▷ construct new MPS tensors

14:     (,) $\leftarrow$ (,)   ▷ apply transfer matrix $\hat{T}_M$

15:      $\leftarrow$ round( )   ▷ construct new $\mathbb{Z}_2$ symmetry operator

16:     (,) $\leftarrow \frac{1}{2}($ $+$, $+$)   ▷ impose $\mathbb{Z}_2$ symmetry (by symmetrization)

17:     **return** (, ,)   ▷ return with A_1, A_2 switched

18: **end function**

One important point is to preserve the $\mathbb{Z}_2$ symmetry under the evolution. The entanglement feature for pure states is $\mathbb{Z}_2$ symmetric, i.e. $W_\rho[\sigma] = W_\rho[-\sigma]$. The symmetry acts on the MPS tensors A_1 and A_2 as

$$\text{} \rightarrow \text{}, \quad \text{} \rightarrow \text{}, \tag{D7}$$

where X and X' are representations of the $\mathbb{Z}_2$ symmetry operator in MPS auxiliary spaces. They must be updated in each iteration with the MPS tensor. Initially, we start with

$$X = \begin{bmatrix} 1 \end{bmatrix}, \tag{D8}$$

which is consistent with the initial setup of A_1, A_2 in Eq. (D6). As new auxiliary degrees of freedom emerge under the singular value decomposition, the $\mathbb{Z}_2$ symmetry action should be calculated. The idea is to transform the $\mathbb{Z}_2$ symmetry action on the old degrees of freedom to the new degrees of freedom by the isometry constructed in SVD. We can show that the following two constructions are equivalent (assuming that the singular values have no accidental degeneracy)

$$\text{} = \text{} = \text{}. \tag{D9}$$

This is the step taken in line 15 of Algorithm 1. The additional round off function is applied to eliminate numerical error accumulated in the calculation, so as to obtain a precise $\mathbb{Z}_2$ symmetry operator X' which squares to identity $X'^2 = \mathbb{I}$ precisely. The symmetry is implemented at each iteration by symmetrizing the MPS tensors A_1, A_2 as shown in line 16 of Algorithm 1.

As we obtain the MPS tensors A_1, A_2 after $2T$ steps of the TEBD iteration (two TEBD iteration correspond to one step of time-evolution in the quantum channel model), we can calculate the entanglement entropy from the entanglement feature $S_{\tilde{\rho}}^{(2)}[\sigma] = -\log(W_\rho[\sigma]/W_\rho[\Uparrow])$. In particular, if we consider a single entanglement region A of
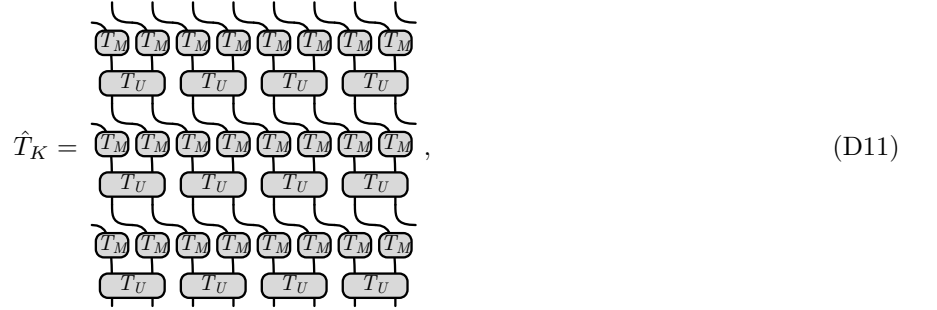
size $|A|$ in a system of N qudits, the entanglement entropy is given by

$$S_{\tilde{\rho}}^{(2)}(A) = \begin{cases} -\log \frac{\text{Tr}(A_1^\downarrow A_2^\downarrow)^{|A|/2}(A_1^\uparrow A_2^\uparrow)^{(N-|A|)/2}}{\text{Tr}(A_1^\uparrow A_2^\uparrow)^{N/2}} & |A| \in \text{even}, \\ -\log \frac{\text{Tr}(A_1^\downarrow A_2^\downarrow)^{(|A|-1)/2}A_1^\downarrow A_2^\uparrow(A_1^\uparrow A_2^\uparrow)^{(N-|A|-1)/2}}{\text{Tr}(A_1^\uparrow A_2^\uparrow)^{N/2}} & |A| \in \text{odd}. \end{cases} \tag{D10}$$

We follow this approach to calculated the entropy growth in Fig. 2(a,b). The calculation is done with the MPS bond dimension cutoff at 64.
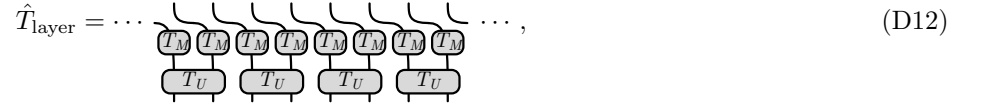
3. VUMPS Approach

In principle, if we follow the TEBD iteration for infinite steps, the MPS should converge to the leading eigenstate $|W_{\rho_\infty}\rangle$ of the transfer matrix. However, the TEBD algorithm is not stable under long-time evolution, as the error rate can not go down due to the SVD truncation at each iteration, hence TEBD is not good for targeting the final state $|W_{\rho_\infty}\rangle$. The VUMPS algorithm was proposed to avoid SVD truncation by variational optimization. To proceed, we first rewrite the transfer matrix into a matrix product operator (MPO) form. We notice that the transfer matrix $\hat{T}_K$ in Eq. (D4) can be deformed to the following form
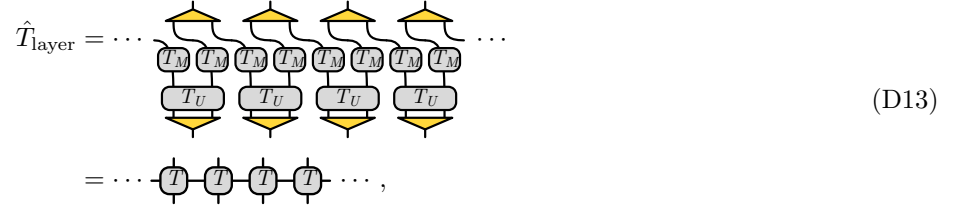
$$\tag{D11}$$

such that the network acquires a one-layer translation symmetry along the time direction. Thus we introduce the single-layer transfer matrix $\hat{T}_{\text{layer}}$,

$$\tag{D12}$$

such that $\hat{T}_K = \hat{T}_{\text{layer}}^{2T}$ for T steps of evolution. We further notice that each $\hat{T}_{U_{ij}}$ operator comes with a projection operator $(1 + Z_i Z_j)/2$, such that only the $Z_{2j-1}Z_{2j} = +1$ states can survive the projection across neighboring layers. Thus we can restrict ourselves to the subspace of $\forall j : Z_{2j-1}Z_{2j} = +1$ and simplify the transfer matrix $\hat{T}_{\text{layer}}$ to

$$\tag{D13}$$

where each yellow triangle denotes a projection operator that projects to the $Z_{2j-1}Z_{2j} = +1$ subspace. In this way, the layer transfer matrix $\hat{T}_{\text{layer}}$ can be written as an MPO, with the MPO tensor given by

$$\tag{D14}$$

Arranging the legs following the order of up, down, left and right, the four-leg MPO tensor T can be represented in the following tensor form

$$T = \begin{bmatrix} \begin{bmatrix} a & 0 \\ c & 0 \end{bmatrix} & \begin{bmatrix} b & 0 \\ c & 0 \end{bmatrix} \\ \\ \begin{bmatrix} 0 & c \\ 0 & b \end{bmatrix} & \begin{bmatrix} 0 & c \\ 0 & a \end{bmatrix} \end{bmatrix}, \tag{D15}$$

with tensor elements specified by

$$\begin{aligned} a &= \frac{(d+1-p)(d^2+(d-1)p+1)}{(d+1)(d^2+1)}, \\ b &= \frac{d^2 p((d-1)p+2)}{(d+1)(d^2+1)}, \\ c &= \frac{d((d-1)p+1)}{d^2+1}, \end{aligned} \tag{D16}$$

where d is the qudit dimension and p is the measurement strength. They are the only two tuning parameters of the random quantum channel model. Having specified the MPO tensor T, we can find the MPS representation of the leading eigenstate $|W_{\rho_\infty}\rangle$ of the layer transfer matrix $\hat{T}_{\text{layer}}$ using the VUMPS algorithm as described in Algorithm 2.

Algorithm 2 Applying VUMPS to find the MPS of the leading eigenstate $|W_{\rho_\infty}\rangle$

---

input: $\hat{T}_{\text{layer}} = \cdots$ $\cdots$ - MPO representation of the layer transfer matrix.

output: $|W_{\rho_\infty}\rangle = \cdots$ $\cdots$ - canonicalized MPS representation of the leading eigenstate of the layer transfer matrix.

1: **procedure** VUMPS
2: ▷ initialize MPS tensors
3:     **while** (A_L, C, A_R) not converge **do** ▷ iterate to improve MPS tensors
4:      $\leftarrow$ VUMPS.iterate
5:     **end while**
6:     **return**
7: **end procedure**

8: **function** VUMPS.ITERATE(A_L, C, A_R)
9:      $\leftarrow (A_L, C, A_R)$ ▷ import MPS tensors
10:     **while** (T_L, T_R) not converge **do**
11:      $\leftarrow$ normalize ▷ power iteration to find the leading left-environment tensor T_L
12:      $\leftarrow$ normalize ▷ power iteration to find the leading right-environment tensors T_R
13:     **end while**
14:     **while** (C, B) not converge **do**
15:      $\leftarrow$ normalize ▷ power iteration to find the leading MPS central tensor C

16:      $\boxed{B} \leftarrow \text{normalize}\left(\begin{array}{c} T_L \; T \; T_R \\ B \end{array} \right)$ ▷ power iteration to find the leading MPS block tensor B

17:      **end while**

18:      $\boxed{A_L} \leftarrow \text{minimize}(\| \boxed{A_L}\boxed{C} - \boxed{B} \|, \text{ subject to } \begin{array}{c} A_L \\ A_L \end{array} = \big| \; \big)$ ▷ optimize the left-isometry tensor A_L

19:      $\boxed{A_R} \leftarrow \text{minimize}(\| \boxed{C}\boxed{A_R} - \boxed{B} \|, \text{ subject to } \begin{array}{c} A_R \\ A_R \end{array} = \big| \;)$ ▷ optimize the right-isometry tensor A_R

20:      $(\boxed{A_L}, \boxed{C}, \boxed{A_R}) \leftarrow \frac{1}{2}(\boxed{A_L} + \boxed{X}\overset{\sigma^x}{\boxed{A_L}}\boxed{X}, \; \boxed{C} + \boxed{X}\boxed{C}\boxed{X}, \; \boxed{A_R} + \boxed{X}\overset{\sigma^x}{\boxed{A_R}}\boxed{X})$ ▷ impose $\mathbb{Z}_2$
symmetry (by symmetrization)

21:      **return** $(\boxed{A_L}, \boxed{C}, \boxed{A_R})$

22: **end function**

The VUMPS works with a canonicalized MPS, meaning that the MPS consists of left-isometry tensors A_L, right-isometry tensors A_R and a central tensor C, as follows

$$|W_{\rho_\infty}\rangle = \cdots \boxed{A_L}\boxed{A_L}\boxed{C}\boxed{A_R}\boxed{A_R} \cdots \,, \tag{D17}$$

where little arrows mark the direction of isometry map (mapping from large space into smaller space). The isometry tensors are initialized to

$$\boxed{A_L} = \underset{\triangledown}{\equiv}, \quad \boxed{A_R} = \underset{\triangledown}{\equiv}, \tag{D18}$$

where each thin line denotes a 2-dimensional space (i.e. a qubit). The auxiliary space contains n qubits and is of the dimension 2^n, where n is a hyper-parameter that can be adjusted. Larger n (larger bond dimension) will generally result in better MPS representation. The isometry tensors initially collect the physical legs of n MPO tensors T away from the center. The little yellow triangle is taken to be a $\mathbb{Z}_2$ symmetric qubit state $(|0\rangle + |1\rangle)/\sqrt{2}$, which is introduced to "ground" the physical legs of MPO tensors more than n steps away from the center. The central tensor C is simply taken to be an identity operator in the n-qubit auxiliary space. The initial ansatz is such chosen to preserve the $\mathbb{Z}_2$ symmetry from the beginning. The symmetry acts on the tensors as

$$\boxed{A_L} \to \boxed{X}\overset{\sigma^x}{\boxed{A_L}}\boxed{X}, \quad \boxed{C} \to \boxed{X}\boxed{C}\boxed{X}, \quad \boxed{A_R} \to \boxed{X}\overset{\sigma^x}{\boxed{A_R}}\boxed{X}, \tag{D19}$$

where $X = \prod_{i=1}^{n} \sigma_i^x$ is the representation of the $\mathbb{Z}_2$ symmetry operator in the auxiliary space. The operator X is fixed under VUMPS iteration, because VUMPS is a variational approach which does not reshuffle existing basis or generate new basis. We impose the $\mathbb{Z}_2$ symmetry by explicit symmetrization in line 20 of Algorithm 2. A key step in the algorithm is to efficiently reconstruct A_L, A_R by solving the optimization problem in line 18, 19 of Algorithm 2. We direct the reader to Ref. 49 for details about how the solution can be approximately constructed in a robust manner.

4. Extracting Volume-Law Coefficient

As the VUMPS iteration converges, we obtain the tensors A_L, C and A_R which are needed to construct the canonicalized MPS state $|W_{\rho_\infty}\rangle$. We can then study all entanglement features of the final state produced by the random quantum channel. In particular, we can extract the volume-law coefficient f which is defined via the scaling of entanglement entropy $S_{\rho_\infty}^{(2)}(A) = (f \log d)|A| + \cdots$ in the $|A| \to \infty$ limit. We first solve the eigen problem of $A_L^\uparrow$ and $A_R^\uparrow$ (note that the isometry is assumed to go from the column space to the row space for $A_L^\uparrow$ and $A_R^\uparrow$),

$$\begin{aligned} A_L^\uparrow |\lambda_{Lm}\rangle &= \lambda_{Lm} |\lambda_{Lm}\rangle, \\ A_R^\uparrow |\lambda_{Rm}\rangle &= \lambda_{Rm} |\lambda_{Rm}\rangle, \end{aligned} \tag{D20}$$

where $m = 0, 1, 2, \cdots$ labels the eigenvalues in a descending order $\lambda_{L0} \geqslant \lambda_{L1} \geqslant \lambda_{L2} \geqslant \cdots$. In fact, only the first two eigenvalues will be needed. Due to the $\mathbb{Z}_2$ symmetry, the eigenstates of $A_L^\downarrow$ ($A_R^\downarrow$) are related to that of $A_L^\uparrow$ ($A_R^\uparrow$) as $X|\lambda_{Lm}\rangle$ ($X|\lambda_{Rm}\rangle$) by applying the symmetry operator X, and the corresponding eigenvalues must be the same. There is also a reflection symmetry about the center, which relates the eigenvalues between $A_L^\uparrow$ and $A_R^\uparrow$ such that $\lambda_{Lm} = \lambda_{Rm} = \lambda_m$. Numerically there is often a slight difference between λ_{Lm} and λ_{Rm} due to the numerical error, so we define $\lambda_m = \sqrt{\lambda_{Lm}\lambda_{Lm}}$ as their geometric mean in practice. Given the setup, we can evaluate the entanglement feature for a region A of size $|A|$ in a system of N qudits,

$$W_{\rho_\infty}(A) = \langle +| (A_L^{\downarrow\mathsf{T}})^{|A|/2} C (A_R^\uparrow)^{(N-|A|)/2} |+\rangle, \tag{D21}$$

where $|+\rangle$ specifies the boundary condition for the MPS. The choice of $|+\rangle$ will not be important in the thermodynamic limit (as $|A|, N \to \infty$), because only the leading eigenstate dominates in the end. We only require $|+\rangle$ to be a $\mathbb{Z}_2$ symmetric state (i.e. $X|+\rangle = |+\rangle$). For example, $|+\rangle = (1+X)|0\rangle$ is a possible choice. Using the $\mathbb{Z}_2$ symmetry property $A_L^\downarrow = X A_L^\uparrow X$ and $X^2 = \mathbb{I}$, Eq. (D21) can be written as

$$\begin{aligned} W_{\rho_\infty}(A) &= \langle +| (X A_L^{\uparrow\mathsf{T}} X)^{|A|/2} C (A_R^\uparrow)^{(N-|A|)/2} |+\rangle \\ &= \langle +| X (A_L^{\uparrow\mathsf{T}})^{|A|/2} X C (A_R^\uparrow)^{(N-|A|)/2} |+\rangle \\ &= \langle +| (A_L^{\uparrow\mathsf{T}})^{|A|/2} X C (A_R^\uparrow)^{(N-|A|)/2} |+\rangle. \end{aligned} \tag{D22}$$

Here we have assumed that both $|A|$ and N are even in sites, which means that they are integer in unit-cells. In this way, the entanglement cut will always pass between unit-cells, which simplifies our calculation. For the purpose of calculating the volume-law coefficient, such choice of entanglement cut does not affect the result. Suppose the state $|+\rangle$ admits the following decomposition $|+\rangle = \sum_m c_{Lm} |\lambda_{Lm}\rangle = \sum_m c_{Rm} |\lambda_{Rm}\rangle$ on the eigenstates with some (unimportant) coefficients c_{Lm} and c_{Rm}, then Eq. (D22) becomes

$$W_{\rho_\infty}(A) = \sum_{m,m'} c_{Lm} c_{Rm'} \lambda_m^{|A|/2} \lambda_{m'}^{(N-|A|)/2} \langle \lambda_{Lm}| X C |\lambda_{Rm'}\rangle. \tag{D23}$$

The entanglement entropy is given by

$$S_{\tilde\rho_\infty}^{(2)}(A) = -\log \frac{W_{\rho_\infty}(A)}{W_{\rho_\infty}(\emptyset)}. \tag{D24}$$

We are interested in its slope with respect to $|A|$, thus we take the derivative

$$\begin{aligned} \partial_{|A|} S_{\tilde\rho_\infty}^{(2)}(A) &= -\frac{\partial_{|A|} W_{\rho_\infty}(A)}{W_{\rho_\infty}(A)} \\ &= -\frac{\sum_{m,m'} c_{Lm} c_{Rm'} \lambda_m^{|A|/2} \lambda_{m'}^{(N-|A|)/2} (\log \lambda_m - \log \lambda_{m'}) \langle \lambda_{Lm}| X C |\lambda_{Rm'}\rangle}{2 \sum_{m,m'} c_{Lm} c_{Rm'} \lambda_m^{|A|/2} \lambda_{m'}^{(N-|A|)/2} \langle \lambda_{Lm}| X C |\lambda_{Rm'}\rangle}. \end{aligned} \tag{D25}$$

We take the thermodynamic limit $|A|, N \to \infty$ but fix the ratio $|A|/N \ll 1$ to be small, Eq. (D25) will be dominated by the leading power ($m = m' = 0$) and the sub-leading power ($m = 1, m' = 0$),

$$\begin{aligned} \partial_{|A|} S_{\tilde\rho_\infty}^{(2)}(A) &= -\frac{c_{L1} c_{R0} \lambda_1^{|A|/2} \lambda_0^{(N-|A|)/2} (\log \lambda_1 - \log \lambda_0) \langle \lambda_{L1}| X C |\lambda_{R0}\rangle}{2 (c_{L0} c_{R0} \lambda_0^{N/2} \langle \lambda_{L0}| X C |\lambda_{R0}\rangle + c_{L1} c_{R0} \lambda_1^{|A|/2} \lambda_0^{(N-|A|)/2} \langle \lambda_{L1}| X C |\lambda_{R0}\rangle)} \\ &= \frac{1}{2} \frac{\log(\lambda_0/\lambda_1)}{\frac{c_{L0} \langle \lambda_{L0}| X C |\lambda_{R0}\rangle}{c_{L1} \langle \lambda_{L1}| X C |\lambda_{R0}\rangle} (\frac{\lambda_0}{\lambda_1})^{|A|/2} + 1}. \end{aligned} \tag{D26}$$

The behavior of $\partial_{|A|} S_{\tilde\rho_\infty}^{(2)}(A)$ in the $|A| \to \infty$ limit crucially depends on whether or not $\frac{c_{L0} \langle \lambda_{L0}| X C |\lambda_{R0}\rangle}{c_{L1} \langle \lambda_{L1}| X C |\lambda_{R0}\rangle}$ vanishes or not. On general ground, c_{L0} would not vanish, because it is a boundary condition that is chosen with some arbitrariness. So it all depends on the inner product $\langle \lambda_{L0}| X C |\lambda_{R0}\rangle$. If $\langle \lambda_{L0}| X C |\lambda_{R0}\rangle = 0$, then $\partial_{|A|} S_{\tilde\rho_\infty}^{(2)}(A) = \frac{1}{2} \log(\lambda_0/\lambda_1)$. If $\langle \lambda_{L0}| X C |\lambda_{R0}\rangle \neq 0$, then as $|A| \to \infty$ the power $(\lambda_0/\lambda_1)^{|A|/2} \to \infty$ diverges, hence $\partial_{|A|} S_{\tilde\rho_\infty}^{(2)}(A) = 0$. Therefore, the volume-law coefficient is determined by

$$f = \lim_{|A| \to \infty} \frac{\partial_{|A|} S_{\tilde\rho_\infty}^{(2)}(A)}{\log d} = \begin{cases} \frac{1}{2} \log_d(\lambda_0/\lambda_1) & \langle \lambda_{L0}| X C |\lambda_{R0}\rangle = 0, \\ 0 & \langle \lambda_{L0}| X C |\lambda_{R0}\rangle \neq 0. \end{cases} \tag{D27}$$

Using this formula, we calculated the volume-law coefficient for different measurement strength p and different qudit dimension d, and the result is shown in Fig. 2(c).

Now we explain our calculation of the measurement-induced entropy drop $\Delta S_x^{(2)}(A)$ and the qudit-environment mutual information $I_\rho(x : A)$. Via the VUMPS algorithm, we have obtained the final entanglement feature state $|W_{\rho_\infty}\rangle$ as the leading eigenstate of $\hat{T}_K$ in Eq. (D4). Note that the last step of $\hat{T}_K$ is a layer of $\hat{T}_M$ (measurement). The state prepared by $\hat{T}_K$ is not quite what we want, because the qudits have been uniformly measured in the last step, then further probing the state with local measurement will double the effect of measurement and can not reflect the actual measurement-induced entropy drop right after the application of unitary gates. In order to prepare a "fresh" state right after the unitary layer, we apply an additional layer of unitary gate transfer matrix to the MPS state to construct the following entanglement feature state

$$|W_\rho\rangle = \cdots \qquad \cdots . \tag{D28}$$

Now we can probe the system with a single-site measurement of strength p. This amounts to applying the transfer matrix $\hat{T}_{M_x}$ to $|W_\rho\rangle$ at site x,

$$\hat{T}_{M_x} |W_\rho\rangle = \cdots \qquad \cdots . \tag{D29}$$

We can then compare the difference of entanglement entropies before and after the measurement in a region A that encloses the site x,

$$\Delta S_x^{(2)}(A) = -\log \frac{\langle A|\hat{T}_{M_x}|W_\rho\rangle}{\langle \Uparrow |\hat{T}_{M_x}|W_\rho\rangle} + \log \frac{\langle A|W_\rho\rangle}{\langle \Uparrow |W_\rho\rangle}. \tag{D30}$$

As explained in Appendix F, this entropy drop is closely related to the qudit-environment mutual information $I_\rho(\{x\} : \bar{A})$, defined via

$$e^{I_\rho(\{x\}:\bar{A})} = \frac{\langle A|X_x|W_\rho\rangle \langle \Uparrow |W_\rho\rangle}{\langle A|W_\rho\rangle \langle \Uparrow |X_x|W_\rho\rangle}, \tag{D31}$$

We will leave the explanations of Eq. (D30) and Eq. (D31) to Appendix F and focus on how to evaluate these quantities from the numerically obtained MPS in this appendix.

To help our calculation, we need to first define the following matrices

$$A_R^{T_M\uparrow} = \qquad , \quad A_R^{T_M\downarrow} = \qquad ; \quad A_R^{\uparrow\downarrow} = \qquad , \quad A_R^{\downarrow\uparrow} = \qquad . \tag{D32}$$

In fact, they are related by $\mathbb{Z}_2$ symmetry: $A_R^{T_M\downarrow} = X A_R^{T_M\uparrow} X$ and $A_R^{\downarrow\uparrow} = X A_R^{\uparrow\downarrow} X$. With these notations, we have

$$
\begin{aligned}
\langle \Uparrow |W_\rho\rangle &= \langle \lambda_{L0}|C|\lambda_{R0}\rangle, \\
\langle \Uparrow |\hat{T}_{M_x}|W_\rho\rangle &= \lambda_0^{-1} \langle \lambda_{L0}|C A_R^{T_M\uparrow}|\lambda_{R0}\rangle, \\
\langle \Uparrow |X_x|W_\rho\rangle &= \lambda_0^{-1} \langle \lambda_{L0}|C A_R^{\downarrow\uparrow}|\lambda_{R0}\rangle, \\
\langle A|W_\rho\rangle &= \lambda_0^{-|A|/2} \langle \lambda_{L0}|C (A_R^\downarrow)^{|A|/2}|\lambda_{R0}\rangle, \\
\langle A|\hat{T}_{M_x}|W_\rho\rangle &= \lambda_0^{-|A|/2} \langle \lambda_{L0}|(A_L^{\downarrow\intercal})^{(x-1)/2} C A_R^{T_M\downarrow}(A_R^\downarrow)^{(|A|-x-1)/2}|\lambda_{R0}\rangle, \\
\langle A|X_x|W_\rho\rangle &= \lambda_0^{-|A|/2} \langle \lambda_{L0}|(A_L^{\downarrow\intercal})^{(x-1)/2} C A_R^{\uparrow\downarrow}(A_R^\downarrow)^{(|A|-x-1)/2}|\lambda_{R0}\rangle.
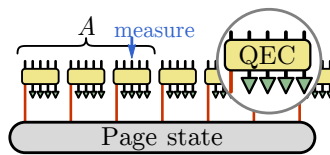\end{aligned}
\tag{D33}
$$

FIG. 13. Five-qubit code toy model.

We have assumed that the region A is embedded in a infinitely large system such that the boundary condition at the entanglement cuts are given by the eigenstates $\langle\lambda_{L0}|$ and $|\lambda_{R0}\rangle$. Here x is an integer labeling the position of the measurement site with respect to the entanglement cut. We assume that x is odd to avoid more tedious discussion of the even-odd effect. For the purpose of studying the scaling behavior with respect to x, it is fine to probe only the odd sites. Given the expressions in Eq. (D33), Eq. (D30) and Eq. (D31) can be evaluated from the MPS tensors A_L, C and A_R. Following this approach, we calculated $\Delta S_x^{(2)}(A)$ and $I_\rho(x:A)$ at $d=2$ and $p=0.1$, using the MPS ansatz with bond dimension 64 (i.e. $n=6$). The result is shown in Fig. 3(c).

Appendix E: Argument for Quantum Error Correcting Volume-Law State

In this section, we give a self-consistent argument on the relation between the measurement-doped unitary circuit and quantum error correction. Our argument is directly motivated by toy examples, including the five-qubit code, holographic codes, and more general stabilizer codes, but applies more generally without referring to any microscopic details.

1. Toy examples

In this section, we describes two toy examples of error correcting states. Despite some differences, both constructions produce a sub-thermal volume-law state, the entanglement of which is robust against moderate amount of measurement.

Five-qubit code The first toy example is constructed by taking a Page state and encode each qubit into five qubits by the 5-qubit QEC code, as depicted in Fig. 13. The state exhibits a volume-law entanglement with $f=1/5$ on average and is stable against any measurement that acts on less than three qubits in every 5-qubit group. The QEC layer protects the quantum information of the Page state from being accessed by local measurements, hence the entanglement entropy can remain unchanged under measurements.

From this example, it is clear that such behavior is only possible in the sub-thermal volume-law state with $f<1$, because it is those $(1-f)$ fraction of qubits that serve as the syndrome bits to enable QEC encoding of the Page state. Noticing that the code distance for the whole layer is only three, this state is not robust against probabilistic measurement. We need different blocks to have correlation, which inspires the next example.

Holographic code The second toy example is constructed by a random tensor network (RTN). Consider a system of N qudits (each qudit is of Hilbert space dimension d), the Page state of these qudits admits a simple RTN representation as shown in Fig. 14(a), where all physical legs are connected to a big random tensor $T_{\alpha_1\alpha_2\cdots\alpha_N}$ in the center. More precisely, the random tensor T discribes the coefficient of the Page state when it is represented on a set of many-qudit basis states,

$$|\Psi_{\text{Page}}\rangle = \prod_{i=1}^{N}\sum_{\alpha_i=1}^{d} T_{\alpha_1\alpha_2\cdots\alpha_N} |\alpha_1\rangle \otimes |\alpha_2\rangle \cdots \otimes |\alpha_N\rangle, \tag{E1}$$

where each tensor element in T is randomly drawn from independent Gaussian distributions. Now we protect the Page state by one additional layer of matrix product operators (MPO) as shown in Fig. 14(b).

$$|\Psi_{\text{sub-Page}}\rangle = \prod_{i=1}^{N}\sum_{\beta_i=1}^{d_1} \hat{O}_{\beta_1}^{\beta_N}\hat{O}_{\beta_2}^{\beta_1}\cdots\hat{O}_{\beta_N}^{\beta_{N-1}} |\Psi_{\text{Page}}\rangle, \tag{E2}$$

where $\hat{O}^{\beta_i}_{\beta_{i+1}} = \sum_{\alpha_i,\alpha'_i} |\alpha_i\rangle O^{\beta_i}_{\beta_{i+1}\alpha_i\alpha'_i} \langle\alpha'_i|$ is the operator acting on the ith qudit as specified by 4-leg tensors of the form $O^{\beta}_{\beta'\alpha\alpha'}$ and is also randomly drawn.
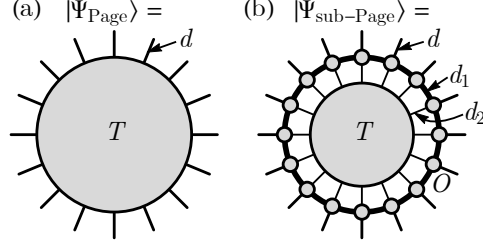

FIG. 14. Random tensor network representations of (a) Page states and (b) sub-Page states. The qudit dimension is d. Bond dimensions of the matrix product operator are specified by d_1 and d_2, assuming $d_1 > d > d_2$.

As the tensors are random, the only relevant parameters of the MPO are its bond dimensions. As specified in Fig. 14(b), we require the bond dimensions to satisfy the hierarchy $d_2 < d$ (modeling introducing extra ancilla) and $d_1 > d$ (modeling a few layers of local unitary circuit) The resulting state, called the sub-Page state in our discussion, is by construction sub-thermal and is robust against projective measurement.

Let us consider a subsystem, which is denoted by the red arrow in Fig. 15, and the measurement on it. For the Page state, any single measurement will disentangle the qudit from the rest of the system, and the entanglement cut will redirect itself to go through the projection operator, therefore the entropy drops by $\log d$, as shown in Fig. 15 (a). However, for the sub-Page state, the entanglement cut will remain unchanged as shown in Fig. 15 (b). If d_1 is sufficiently large such that we have $2\log d_1 > \log d_2$, any attempt to cut through the projection operator will have more cost more, as shown in Fig. 15 (c). In this case, the measurement does not result in any drop of the entanglement entropy. So the central page state can be protected from local measurements just by a layer of MPO with sufficiently large bond dimension $d_1 > \sqrt{d_2}$. We can treat this layer of MPO as a QEC encoding circuit (in fact, random tensors are asymptotically perfect, meaning that they automatically approximate QEC codes). This model works as long as $d_2 < d$, i.e. the volume law fraction $f = \log(d_2/d) < 1$.
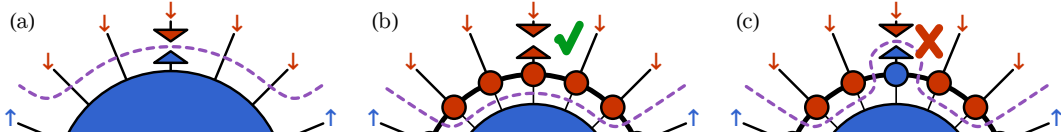

FIG. 15. Response to the measurement for (a) the Page state and (b) the sub-Page state. The case shown in (c) is prohibited as long as $d_1 > \sqrt{d_2}$.

2. General argument

In this section, we provide the general argument on why the final state can be understood by error correction. As depicted in Fig. 3 (a), we assume that the volume-law piece of the entanglement entropy of the final state completely comes from that of the input Page state. Namely, the QECC layer, regarded as a unitary transformation from the tensor product of the Page state and ancilla $|\psi\rangle \otimes |0\cdots0\rangle$ to the final state $|\chi\rangle$, does *not* increase the entanglement entropy of the original state by a volume-law amount. This locality constraint leads to the assumption that any large enough subsystem A can have stabilizers that only have support on A.

This provides a natural mechanism to protect the entanglement from measurement, which is explained as follows. Let us call the final state $|\chi\rangle = T_{QECC} |\psi\rangle$ and consider the reduced density matrix for a large enough subsystem A. When measurements of of t qubits happen in A, we can decompose the corresponding projection operator into a sum of Pauli strings as

$$P_{i_1} P_{i_2} \cdots P_{i_t} = \mathcal{N}\left(\mathbb{I} + \sum_s c_s \mathcal{O}_s\right), \tag{E3}$$

where $\mathcal{N}$ is a normalization factor and $\mathcal{O}_s$ represents a Pauli string with weight equal or less than t. Accordingly, the purity of ρ_A after the measurement can also be written as the following sum

$$\mathrm{Tr}\,\rho_{A,after}^2 = \sum_{O_i,\tilde{O}_i} \left[\vcenter{\hbox{\includegraphics{}}}\right] = \sum_{\mathcal{O},\tilde{\mathcal{O}}} \left[\vcenter{\hbox{\includegraphics{}}}\right], \tag{E4}$$

where we introduce $\mathcal{O} = \mathcal{O}_1\tilde{\mathcal{O}}_1$ and $\tilde{\mathcal{O}} = \mathcal{O}_2\tilde{\mathcal{O}}_2$. Now we assume $\mathcal{O}$ and $\tilde{\mathcal{O}}$ are detectable errors, which implies that they anti-commute with at least one stabilizer. When $\mathcal{O}$ and $\tilde{\mathcal{O}}$ are deep in the bulk of A, such stabilizers are fully supported in A (they exist by assumption) and we can have for example
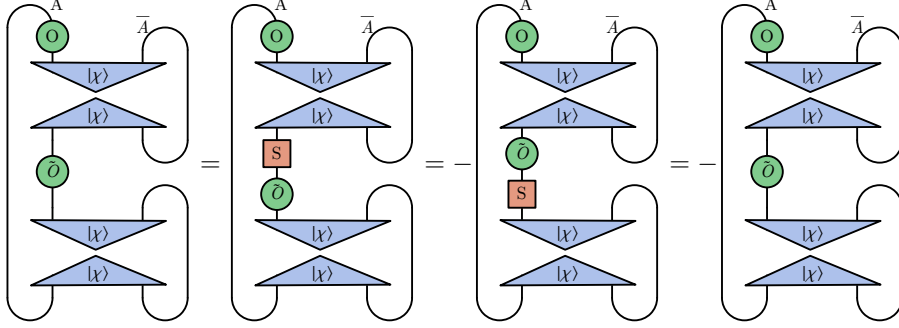
for $\tilde{\mathcal{O}} \neq \mathbb{I}$, which directly shows that such kind of terms vanishes. Similar calculation is true for $\mathcal{O}$. The exceptions are when $\mathcal{O}$ or $\tilde{\mathcal{O}}$ are near the boundary of A and the stabilizers may have support in both A and $\bar{A}$. It is easy to see that this argument still holds when the measurement is in $\bar{A}$ or both A and $\bar{A}$.

More rigorously, we may consider a stabilizer QECC that can correct for any weight-t Pauli error. Consider the reduced density matrix for a subsystem A in the codespace $\rho_A \equiv \mathrm{Tr}_{\bar{A}}(\Pi_{\text{codespace}})$ where $\Pi_{\text{codespace}}$ is the projector onto states in the codespace. We now perform $m \leq t$ single-qubit measurements in the Pauli basis, so that the new reduced density matrix is given by $\sigma_A \propto \Pi_A\rho_A\Pi_A$, where Π_A is a product of m single-qubit projectors in the Pauli basis. We may expand Π_A as

$$\Pi_A = \frac{1}{2^m}\left[1 + \sum_{j=1}^{2^m-1} \mathcal{E}_j\right]. \tag{E5}$$

where $\{\mathcal{E}_j\}$ are Pauli operators. As we prove in the following section, the second Rényi entropy $S^{(2)}(\rho_A) \equiv -\log_2 \mathrm{Tr}(\rho_A^2)$ is related to the entanglement for the same subsystem, after performing these m single-qubit measurements in the Pauli basis, as

$$S^{(2)}(\sigma_A) = S^{(2)}(\rho_A) - \log_2[1 + n_A] \tag{E6}$$

where n_A is the number of Pauli operators in the set $\{\mathcal{E}_j\}$ that have syndromes which cannot be determined by performing measurements of stabilizers that are exclusively within the A subsystem. Assuming that the stabilizers have a finite average size, the quantity n_A will scale exponentially in the number of measurements that are performed near the boundary of region A, so that the right-hand side of Eq. (E6) will only provide an area-law correction to the Rényi entropy.

If we roughly use pN as the number of measurement in each round, then the code distance has to be larger than pN. Notice that the length of the stabilizers is not tightly constrained by the code distance. Therefore, although the code distance is macroscopic, the stabilizers can still have a microscopic length for our argument to work.

For this mechanism to continue work, all the errors have to be corrected by the next layer of unitary evolution, namely all the Pauli strings in the measurements are correctable errors. Therefore, the code distance has to be larger than $2pN$. If we assume the code distance is exactly $2pN$ (as well as the code being non-degenerate), then we can derive the Hamming bound shown in the main text.

Eq. (E6) can also be used to argue for the power-law decrease in the entanglement entropy when performing a measurement a distance x from the boundary of a subsystem, in the sub-thermal volume-law phase that is obtained for Clifford dynamics with measurements in the Pauli basis. This is because Eq. (E6) also holds for any stabilizer state in which a single-qubit measurement has no overlap with the stabilizer group. Consider a semi-infinite region A. For the sub-thermal volume law state generated by random Clifford dynamics with measurements, let $p(x)$ be the probability that a single-qubit measurement, performed a distance x from the boundary of A commutes with all operators that stabilize the state, and that lie entirely within in the A subsystem. From Eq. (E6), the average entanglement entropy drop after this measurement is exactly

$$
\begin{aligned}
\overline{\Delta S(x)} &\equiv [1 - p(x)] \log_2(1) + \log_2(2) p(x) \\
&= p(x).
\end{aligned}
\tag{E7}
$$

Therefore, if $p(x)$ falls faster than $1/x$, then the the entanglement drop after performing a finite density of measurements will be a *constant*.

We estimate $p(x)$ using the known stabilizer length distribution $P(\ell)$ in random Clifford circuits, with measurements in the Pauli basis [26]. In the volume-law phase, it is known [26] that $P(\ell) = \alpha(p)\ell^{-2} + s(p)\delta(\ell - (L/2))$ in a system with size L. We now consider a region A defined by the interval $[1, |A|]$, and we perform a measurement at a position x such that $1 \ll x \ll |A|$ where we perform a single measurement. The number of stabilizers that are contained entirely within A, and that have "crossed" the position x, i.e. that have their left endpoint $y_L < x$ and their right endpoint $y_R > x$ is

$$
N(x) \equiv \int_0^x \int_x^{|A|} dy_L \, dy_R \, P(|y_L - y_R|) = \alpha \ln(x) + O(x/|A|)
\tag{E8}
$$

The probability that all of these stabilizers commute with the single-qubit measurement is exponentially small in the number of stabilizers, which gives an estimate of $p(x) \sim e^{-N(x)} = x^{-\alpha}$. This then gives the power-law decay $\overline{\Delta S(x)} \sim x^{-\alpha}$ for the entanglement with the distance that the measurement is performed, from the boundary. The precise exponent for this power-law behavior cannot be determined without knowing more detailed properties of the stabilizers. For example, if we assume that the stabilizers drawn from the distribution $P(\ell)$ have equal probability of acting as a Pauli X, Y, Z, or the identity I at site x, then the probability $p(x) = 2^{-N(x)} = x^{-\alpha \ln(2)}$.

3. Proof of Eq. (E6)

Let the tensor T be the encoding of a state on k qubits into a state on N qubits with a stabilizer quantum error-correcting code (QECC). We assume that this encoding is a valid quantum error-correcting code (QECC) with code distance d; the code can then correct for any Pauli error of weight $t \leq \lfloor (d-1)/2 \rfloor$. Since $T : \mathbb{C}^{2^k} \to \mathbb{C}^{2^N}$ is a valid encoding map for a QECC, it is isometric $T^\dagger T = 1_{2^k \times 2^k}$.

We now consider the density matrix

$$
\rho \equiv T T^\dagger
\tag{E9}
$$

which is a projector onto the codespace of the QECC. We further bipartition the N spins into an A subsystem, and its complement $\bar{A}$, and define the reduced density matrix $\rho_A \equiv \mathrm{Tr}_{\bar{A}}(T T^\dagger)$. If G is the Pauli stabilizer group for the QECC, then the reduced density matrix may be equivalently written as

$$
\rho_A = \frac{1}{D_A} \sum_{g \in G_A} g
\tag{E10}
$$

where G_A is the subgroup of G, consisting of elements of the stabilizer group that act as the identity operator on $\bar{A}$, and D_A is the Hilbert space dimension of the A subsystem.

Now, let Π_A be a product of single-qubit projection operators in the Pauli basis, on $m \leq t$ spins in the A subsystem. We may expand Π_A as a sum of Pauli operators as

$$\Pi_A = \frac{1}{2^m}\left[1 + \sum_{j=1}^{2^m-1} \mathcal{E}_j\right]. \tag{E11}$$

We refer to the Pauli operators $\{\mathcal{E}\}$ appearing in this expansion as "errors". Since $m \leq t$, each of these errors are correctable, and we observe that

$$\mathrm{Tr}(\mathcal{E}_j \rho) = 0 \qquad \mathrm{Tr}(\mathcal{E}_i \mathcal{E}_j \rho) = 0 \quad (i \neq j) \tag{E12}$$

As a result, the reduced density matrix for the state, after performing these measurements is

$$\sigma_A \equiv \frac{\Pi_A \rho_A \Pi_A}{\langle \Phi | \Pi_A | \Phi \rangle} = 2^m \Pi_A \rho_A \Pi_A \tag{E13}$$

The purity of σ_A may be expanded as

$$\mathrm{Tr}(\sigma_A^2) = \mathrm{Tr}(\rho_A^2) + 2\sum_j \mathrm{Tr}(\mathcal{E}_j \rho_A) + \sum_{i,j}\mathrm{Tr}(\mathcal{E}_i \rho_A \mathcal{E}_j \rho_A)$$

We observe that $\mathrm{Tr}(\mathcal{E}_j \rho_A) = 0$ due to Eq. (E12).

We evaluate the final term as follows. First, we observe that $\mathrm{Tr}(\mathcal{E}_i \rho_A \mathcal{E}_j \rho_A) = 0$ if either $\mathcal{E}_i$ or $\mathcal{E}_j$ is an error with an *localizable syndrome*, i.e. an error that can be detected via syndrome measurements that act exclusively in the A subsystem. Let $\mathcal{E}_i$ be a localizable error; then there is an element $h \in G_A$, such that $\{h, \mathcal{E}_i\} = 0$. As a result,

$$\begin{aligned}
\mathrm{Tr}(\mathcal{E}_i \rho_A \mathcal{E}_j \rho_A) &= \mathrm{Tr}(\mathcal{E}_i h \rho_A \mathcal{E}_j \rho_A) \\
&= -\mathrm{Tr}(h \mathcal{E}_i \rho_A \mathcal{E}_j \rho_A) = -\mathrm{Tr}(\mathcal{E}_i \rho_A \mathcal{E}_j \rho_A)
\end{aligned} \tag{E14}$$

so that $\mathrm{Tr}(\mathcal{E}_i \rho_A \mathcal{E}_j \rho_A) = 0$. If both $\mathcal{E}_i$ and $\mathcal{E}_j$ cannot be localized, then both errors commute with the stabilizer subgroup G_A, and

$$\mathrm{Tr}(\mathcal{E}_i \rho_A \mathcal{E}_j \rho_A) = \mathrm{Tr}(\mathcal{E}_i \mathcal{E}_j \rho_A^2) = \delta_{ij}\,\mathrm{Tr}(\rho_A^2) \tag{E15}$$

In the last line, we have again used Eq. (E12). Therefore, we conclude that the second Rényi entropy $S^{(2)}(\sigma_A) \equiv -\log_2 \mathrm{Tr}(\sigma_A^2)$ after the measurements is

$$S^{(2)}(\sigma_A) = S^{(2)}(\rho_A) - \log_2[1 + n_A] \tag{E16}$$

where n_A is the number of errors in $\{\mathcal{E}_i\}$ whose syndromes cannot be localized to the A subsystem.

Appendix F: Entropy Drop and Qudit-Environment Information

We propose the qudit-environment mutual information $I_\rho(\{x\} : \bar{A}) = S_{\bar{\rho}}^{(2)}(\{x\}) + S_{\bar{\rho}}^{(2)}(\bar{A}) - S_{\bar{\rho}}^{(2)}(\{x\} \cup \bar{A})$ as a measure of the QEC capacity of the sub-thermal volume-law state. Note that the entanglement entropies are evaluated with respect to the normalized density matrix $\bar{\rho} = \rho / \mathrm{Tr}\,\rho$, such that

$$e^{-S_{\bar{\rho}}^{(2)}(A)} = W_{\bar{\rho}}(A) = \frac{W_\rho(A)}{W_\rho(\emptyset)} = \frac{\langle A | W_\rho \rangle}{\langle \Uparrow | W_\rho \rangle}, \tag{F1}$$

where $|A\rangle = \prod_{i \in A} X_i |\Uparrow\rangle$ is the Ising basis state for region A (i.e. $\sigma_i = \downarrow$ if $i \in A$ and $\sigma_i = \uparrow$ if $i \in \bar{A}$). Using Eq. (F1), it can be shown that

$$\begin{aligned}
e^{I_\rho(\{x\}:\bar{A})} &= e^{S_{\bar{\rho}}^{(2)}(\{x\}) + S_{\bar{\rho}}^{(2)}(\bar{A}) - S_{\bar{\rho}}^{(2)}(\{x\}\cup\bar{A})} \\
&= \frac{e^{-S_{\bar{\rho}}^{(2)}(\{x\}\cup\bar{A})}}{e^{-S_{\bar{\rho}}^{(2)}(\{x\})} e^{-S_{\bar{\rho}}^{(2)}(\bar{A})}} \\
&= \frac{\frac{\langle A | X_x | W_\rho \rangle}{\langle \Uparrow | W_\rho \rangle}}{\frac{\langle \Uparrow | X_x | W_\rho \rangle}{\langle \Uparrow | W_\rho \rangle} \frac{\langle A | W_\rho \rangle}{\langle \Uparrow | W_\rho \rangle}} \\
&= \frac{\langle A | X_x | W_\rho \rangle \langle \Uparrow | W_\rho \rangle}{\langle A | W_\rho \rangle \langle \Uparrow | X_x | W_\rho \rangle},
\end{aligned} \tag{F2}$$

which explains Eq. (12).

Consider making a measurement at position x in region A. Suppose the measurement is described by the operator M_x, its effect on the entanglement feature is implemented by acting the corresponding transfer matrix $\hat{T}_{M_x}$ to the entanglement feature state $|W_\rho\rangle \to \hat{T}_{M_x}|W_\rho\rangle$. According to Eq. (F1), the entanglement entropy of region A after the measurement is given by

$$S_x^{(2)}(A) = -\log \frac{\langle A|\hat{T}_{M_x}|W_\rho\rangle}{\langle \Uparrow |\hat{T}_{M_x}|W_\rho\rangle}, \tag{F3}$$

where the denominator $\langle \Uparrow |\hat{T}_{M_x}|W_\rho\rangle$ provides the appropriate normalization for the entanglement feature state. Therefore the entropy drop after measurement should be defined as

$$\Delta S_x^{(2)}(A) = -\log \frac{\langle A|\hat{T}_{M_x}|W_\rho\rangle}{\langle \Uparrow |\hat{T}_{M_x}|W_\rho\rangle} + \log \frac{\langle A|W_\rho\rangle}{\langle \Uparrow |W_\rho\rangle}, \tag{F4}$$

which is the definition given in Eq. (13).

To derive the relation between the measurement-induced entropy drop $\Delta S_x^{(2)}(A)$ and the qudit-environment mutual information $I_\rho(\{x\} : \bar{A})$, we start with the definition in Eq. (F4),

$$\begin{aligned}
\Delta S_x^{(2)}(A) &\equiv -\log \frac{\langle A|\hat{T}_{M_x}|W_\rho\rangle}{\langle \Uparrow |\hat{T}_{M_x}|W_\rho\rangle} + \log \frac{\langle A|W_\rho\rangle}{\langle \Uparrow |W_\rho\rangle} \\
&= -\log \frac{\langle A|1 - \frac{p}{d+1} + \frac{pd}{d+1}X_x|W_\rho\rangle}{\langle \Uparrow |1 - \frac{p}{d+1} + \frac{pd}{d+1}X_x|W_\rho\rangle} + \log \frac{\langle A|W_\rho\rangle}{\langle \Uparrow |W_\rho\rangle} \\
&= -\log \frac{\langle A|1 + \frac{pd}{d+1-p}X_x|W_\rho\rangle}{\langle \Uparrow |1 + \frac{pd}{d+1-p}X_x|W_\rho\rangle} + \log \frac{\langle A|W_\rho\rangle}{\langle \Uparrow |W_\rho\rangle} \\
&= -\log \left(1 + \frac{pd}{d+1-p}\frac{\langle A|X_x|W_\rho\rangle}{\langle A|W_\rho\rangle}\right) + \log \left(1 + \frac{pd}{d+1-p}\frac{\langle \Uparrow |X_x|W_\rho\rangle}{\langle \Uparrow |W_\rho\rangle}\right),
\end{aligned} \tag{F5}$$

where we have used inserted the definition of $\hat{T}_{M_x}$ in Eq. (C5). Assuming p is small in the weak measurement limit, we expand $\Delta S_x^{(2)}(A)$ in power series of p,

$$\begin{aligned}
\Delta S_x^{(2)}(A) &= -\frac{pd}{d+1}\left(\frac{\langle A|X_x|W_\rho\rangle}{\langle A|W_\rho\rangle} - \frac{\langle \Uparrow |X_x|W_\rho\rangle}{\langle \Uparrow |W_\rho\rangle}\right) + \mathcal{O}(p^2) \\
&= -\frac{pd}{d+1}\frac{\langle \Uparrow |X_x|W_\rho\rangle}{\langle \Uparrow |W_\rho\rangle}\left(\frac{\langle A|X_x|W_\rho\rangle \langle \Uparrow |W_\rho\rangle}{\langle A|W_\rho\rangle \langle \Uparrow |X_x|W_\rho\rangle} - 1\right) + \mathcal{O}(p^2) \\
&= -\frac{pd}{d+1}W_{\bar{\rho}}(\{x\})\left(e^{I_\rho(\{x\}:\bar{A})} - 1\right) + \mathcal{O}(p^2),
\end{aligned} \tag{F6}$$

where $\frac{\langle \Uparrow |X_x|W_\rho\rangle}{\langle \Uparrow |W_\rho\rangle} = W_{\bar{\rho}}(\{x\}) = e^{-S_{\bar{\rho}}^{(2)}(\{x\})}$ is the single-qudit purity (at position x). We have used Eq. (F2) to introduce the exponentiated mutual information $e^{I_\rho(\{x\}:\bar{A})}$. In the volume-law phase, a rough estimate is $S_{\bar{\rho}}^{(2)}(\{x\}) = f\log d$, hence $W_{\bar{\rho}}(\{x\}) = d^{-f}$, therefore

$$\Delta S_x^{(2)}(A) = -p\left(e^{I_\rho(\{x\}:\bar{A})} - 1\right)\frac{d^{1-f}}{d+1} + \mathcal{O}(p^2), \tag{F7}$$

which justifies the relation of Eq. (13). If x is deep in region A, the mutual information $I_\rho(\{x\} : \bar{A})$ is expected to be small. In the limit of $I_\rho(\{x\} : \bar{A}) \to 0$, the entropy drop $\Delta S_x^{(2)}(A)$ directly proportional to the mutual information $I_\rho(\{x\} : \bar{A})$,

$$\Delta S_x^{(2)}(A) \simeq -p\frac{d^{1-f}}{d+1}I_\rho(\{x\} : \bar{A}). \tag{F8}$$

The more the qudit x can inform about the complement region $\bar{A}$, the more entropy drop will be produced by measuring it.

Appendix G: Stability of the Volume-Law Phase in Hybrid Clifford Circuits

In this section, we study the stability of the volume-law entangled phase that emerges in a certain random Clifford circuit with projective measurements. The particular dynamics that we consider are generated by starting with a state of N spin-1/2 degrees of freedom that are initialized in a product state in the Pauli Y basis. The spins are subject to nearest-neighbor, two-site CNOT gates; the "control" qubit is chosen randomly whenever it is applied. These Clifford dynamics generate a high degree of entanglement when acting on states in the Pauli Y basis, as indicated by the blue curve in Fig. 16a, which shows the growth and saturation of the half-system von Neumann entanglement entropy after averaging over realizations of these unitary circuits for $N = 200$ spins. The von Neumann entanglement is given as $\overline{S(t)} = \overline{\text{Tr}[\rho_A \log_2 \rho_A]}$, where A is a subsystem of size $N = 100$, so that the saturating value of the entanglement entropy is nearly maximal.
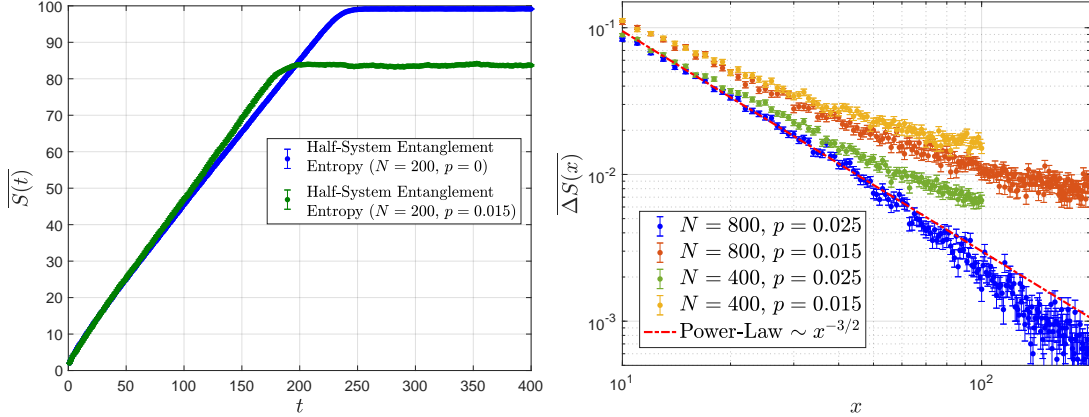

FIG. 16. In the absence of measurements, the Clifford dynamics consisting of CNOT gates applied to an initial product state in the Pauli Y basis leads to the rapid growth of the entanglement. The saturation of the half-system von Neumann entanglement entropy $S = \text{Tr}[\rho \log_2 \rho]$ to near-maximal values for a system of $N = 200$ spins is shown in (a). In the presence of measurements in the Pauli basis, and after evolving the initial state for $O(N)$ timesteps, we probe the reduction in the half-system entanglement entropy after performing measurements at a distance x from the boundary of the subsystem. This is related to the qudit-environment mutual information, as described in the main text. The decay of this change in the entanglement appears qualitatively similar to the power-law behavior $\overline{\Delta S(x)} \sim x^{-3/2}$ for the values of the measurement probabilities shown.

We now include projective measurements in the dynamics. A single timestep of these "hybrid" dynamics now includes a round of two-qubit CNOT gates followed by single-qubit measurements in the Pauli basis. The measurement of each spin is done independently, and with probability p. For sufficiently small p, the entanglement entropy appears to saturate to values that are consistent with a volume-law scaling of the entanglement (e.g. the green curve in Fig. 16a). In the steady-state – after a number of timesteps scaling polynomially in N – we consider the change in the half-system entanglement entropy, after performing a single-qubit measurement at $x \in [0, N/4]$, where the position of the measurement x is relative to the closest boundary of the subsystem. The decrease in the von Neumann entanglement after performing this measurement is averaged over $O(10^4)$ realizations of these dynamics to produce the data in Fig. 16b. This averaged entanglement drop appears to be qualitatively close to the power-law behavior $\overline{\Delta S(x)} \sim x^{-3/2}$ predicted by the entanglement feature description of the volume-law entangled steady-state. This behavior is supposed to emerge when $\xi \ll x \ll N$, where ξ is the correlation length in the Ising model description of the entanglement dynamics, which is very small deep in the volume-law entangled phase. Without knowledge of the precise scaling of the qudit environment mutual information when $x/N \sim O(1)$, we are unable to quantitatively extract the power-law behavior and determine if this power depends on the measurement probability p within the volume-law entangled phase.

Appendix H: Fermionic Gaussian State Approximations

In this section, we give an analytical calculation of the exponent $3/2$ using the free fermion approximation. We start by analyzing the transfer matrices $\hat{T}_{U_{ij}}$ and $\hat{T}_{M_i}$ in Eq. (8). Recall that the entanglement is mapped to Ising spin correlation in the entanglement feature formulation. The unitary gate entangles the nearby sites together, hence

$\hat{T}_{U_{ij}}$ generally promotes the ferromagnetic correlations between neighboring Ising spins. The on-site measurement disentangles the qudit from its environment, hence $\hat{T}_{M_i}$ generally breaks the Ising correlation and disorder the spin. Therefore, it is reasonable to approximate $\hat{T}_{U_{ij}} \simeq e^{JZ_iZ_j}$ and $\hat{T}_{M_i} \simeq e^{hX_i}$ by the imaginary time evolution of Ising coupling and transverse field terms respectively. This approximation allows us to simplify the entanglement dynamics to an imaginary time Floquet problem of quantum Ising model, which can then be mapped to a free fermion Floquet problem and solved analytically. In this way, we can obtain the exponent $3/2$ analytically. In the simplified model, the one-step transfer matrix for the entanglement feature state reads

$$\hat{T}_{\text{step}} = \prod_{i=1}^{N} e^{JZ_iZ_{i+1}} \prod_{i=1}^{N} e^{hX_i} , \tag{H1}$$

where N is the system size assuming the periodic boundary condition. We keep a finite N to regulate the calculation and take the thermodynamic limit $(N \to \infty)$ in the end. The relative ordering between $\hat{T}_{U_{ij}}$ and $\hat{T}_{M_i}$ does not change results qualitatively. Here, we put $\hat{T}_{U_{ij}}$ on the left side of $\hat{T}_{M_i}$, as contrary to the ordering in Eq. (9), such that it prepares a final state suitable for studying the measurement effect. Eq. (H1) imitates a Trotterized $(1+1)$D transverse field Ising model in the imaginary-time and can be exactly solvable by a Jordan-Wigner transformation

$$\chi_{2j-1} = \prod_{1 \leq i < j} X_i Z_j , \quad \chi_{2j} = \prod_{1 \leq i < j} X_i Y_j , \quad j = 1, 2, \cdots, N , \tag{H2}$$

with $\chi_1 = Z_1$ and $\chi_2 = Y_1$. The $\mathbb{Z}_2$ symmetry operator $\prod_i X_i$ of the Ising spins is also the fermion parity operator of the Jordan-Wigner fermions. Since the Ising model is restricted to the $\mathbb{Z}_2$ even sector, the fermions are also in the $\mathbb{Z}_2^F$ even sector with the anti-periodic boundary condition. The transfer matrix rewritten in terms of fermions is

$$\hat{T}_{\text{step}} = \exp\left(iJ \sum_{j=1}^{N} \chi_{2j}\chi_{2j+1} \right) \exp\left(ih \sum_{j=1}^{N} \chi_{2j-1}\chi_{2j} \right) , \quad \chi_{2N+1} = -\chi_1 . \tag{H3}$$

We can diagonalize the transfer matrix using the fermion formalism in the momentum space. We first define the momentum-space fermion operators $c_{k,A}$ and $c_{k,B}$ with two sites (labeled by A and B) per unit cell,

$$\chi_{2j-1} = \frac{1}{\sqrt{N}} \sum_k e^{ijk} c_{k,A} , \quad \chi_{2j} = \frac{1}{\sqrt{N}} \sum_k e^{ijk} c_{k,B} . \tag{H4}$$

The momentum takes the values in $k \in [-\pi, \pi)$ with $k = \frac{2\pi}{N}\left(s + \frac{1}{2}\right), s \in \mathbb{Z}$. For simplicity, N is fixed to be an even number in order to avoid the $k = \pi$ mode. Notice that $c_{k,A/B}$ are complex fermions with the $k < 0$ modes being related to the $k > 0$ modes by $c_{-k,A} = c_{k,A}^\dagger$ and $c_{-k,B} = c_{k,B}^\dagger$, so that the $k < 0$ modes can be excluded to avoid double counting. As a result, the transfer matrix cast in the momentum space can be factorized into a product of each momentum mode

$$\hat{T}_{\text{step}} = \prod_{k>0} \exp\left(-c_k^\dagger h_k^J c_k \right) \exp\left(-c_k^\dagger h_k^h c_k \right) = \prod_{k>0} \hat{T}(k) , \tag{H5}$$

where we have defined $c_k = \binom{c_{k,A}}{c_{k,B}}$ and

$$\begin{aligned} \hat{T}(k) &= \exp\left(-c_k^\dagger h_k^J c_k \right) \exp\left(-c_k^\dagger h_k^h c_k \right) , \\ h_k^J &= J\left(\sin k \sigma^x - \cos k \sigma^y \right) , \\ h_k^h &= h\sigma^y . \end{aligned} \tag{H6}$$

Different momentum modes can be diagonalized separately. Let us introduce

$$a_k = \cosh J \cosh h - e^{ik} \sinh J \sinh h , \quad b_k = \cosh J \sinh h - e^{ik} \sinh J \cosh h . \tag{H7}$$

Then the leading eigenvalue of $\hat{T}(k)$ is given by

$$\lambda_{k,+} = \operatorname{Re} a_k + \sqrt{|b_k|^2 - (\operatorname{Im} a_k)^2}, \tag{H8}$$

and the corresponding leading eigenstate can be written as

$$|W_{\rho_\infty}\rangle \propto \prod_{k>0} |\lambda_{k,+}\rangle = \prod_{k>0} \left(A_k c_{k,A}^\dagger + B_k c_{k,B}^\dagger \right) |\text{vac}\rangle .$$

$$A_k = \mathrm{i} b_k^* , \, B_k = \mathrm{i} \,\text{Im}\, a_k + \sqrt{|b_k|^2 - (\text{Im}\, a_k)^2} ,$$

(H9)

with $|\text{vac}\rangle$ being the vacuum state of $c_{k,A/B}$. One can check that $|W_{\rho_\infty}\rangle$ always has an even fermion parity and thus is indeed a legitimate entanglement feature state (respecting the Ising symmetry $\mathbb{Z}_2$ in the spin language). It will be useful mention that in the limit of $h = 0$, the state $|W_{\rho_\infty}\rangle$ reduces to

$$|W_{h=0}\rangle \propto \prod_{k>0}(-\mathrm{i} e^{-\mathrm{i}k} c_{k,A}^\dagger + c_{k,B}^\dagger) |\text{vac}\rangle ,$$

(H10)

which corresponds to $|W_{h=0}\rangle = |\Uparrow\rangle + |\Downarrow\rangle$ in the spin language, because the transfer matrix contains only the Ising coupling term $\prod_i e^{JZ_i Z_{i+1}}$ in this limit, whose leading eigenstate is the ferromagnetic cat state.

Having found the leading eigenstate $|W_{\rho_\infty}\rangle$ of the transfer matrix $\hat{T}_{\text{step}}$, we can evaluate the entanglement feature in any region A by

$$W_{\bar{\rho}_\infty}(A) = \frac{\langle A | W_{\rho_\infty}\rangle}{\langle \Uparrow | W_{\rho_\infty}\rangle},$$

(H11)

where $|A\rangle = \prod_{i\in A} X_i |\Uparrow\rangle$ encodes the region A and $|\Uparrow\rangle$ is the all-up state in the Ising language. To proceed, we notice that the $\mathbb{Z}_2$ symmetry of the state $|W_{\rho_\infty}\rangle$ allows us to replace $|\Uparrow\rangle$ by its $\mathbb{Z}_2$ symmetric form $|\Uparrow\rangle + |\Downarrow\rangle = |W_{h=0}\rangle$ without affecting the result. This amounts to the following replacements

$$|\Uparrow\rangle \to |W_{h=0}\rangle ,$$

$$|A\rangle = \prod_{i\in A} X_i |\Uparrow\rangle \to \prod_{i\in A} X_i |W_{h=0}\rangle = Z_{i_0} \left(\prod_{i_0 < i < i_1} X_i \right) Z_{i_1} |W_{h=0}\rangle = \mathrm{i}\chi_{2i_0}\chi_{2i_1-1} |W_{h=0}\rangle ,$$

(H12)

where we have assumed the region A to be a single segment strictly between sites i_0 and i_1 (assuming $i_1 > i_0$, such that $|A| = i_1 - i_0 - 1$ counts the size of A). In the above derivation, we are free to insert the $Z_{i_0} Z_{i_1}$ operator because the state $|W_{h=0}\rangle = |\Uparrow\rangle + |\Downarrow\rangle$ has fully correlated that $Z_{i_0} Z_{i_1} |W_{h=0}\rangle = |W_{h=0}\rangle$. Then the string operator dressed by the Z operators can be translated to the fermion bilinear operator following Eq. (H2). Plugging Eq. (H12) into Eq. (H11), we arrive at

$$W_{\bar{\rho}_\infty}(A) = \frac{\langle W_{h=0}|\mathrm{i}\chi_{2i_0}\chi_{2i_1-1}|W_{\rho_\infty}\rangle}{\langle W_{h=0}|W_{\rho_\infty}\rangle} .$$

(H13)

which explains Eq. (14) by taking $i_0 = 0$ and $i_1 = |A| + 1$. One can also choose to insert any of the four combination of Z_{i_0}/Z_{i_0-1} and Z_{i_1}/Z_{i_1+1} and they yield different fermion operators by by construction give the same result. This gauge choice comes from the fact that $|W_{h=0}\rangle$ appears on the left of the correlator. Note that we denote the numerator of Eq. (H13) by $W_{\rho_\infty}(A) = \langle W_{h=0}|\mathrm{i}\chi_{2i_0}\chi_{2i_1-1}|W_{\rho_\infty}\rangle$, which is the unnormalized entanglement feature.

Given the fermion Gaussian states $|W_{\rho_\infty}\rangle$ in Eq. (H9) and $|W_{h=0}\rangle$ in Eq. (H10), it is straightforward to evaluate $W_{\bar{\rho}_\infty}$ in Eq. (H13), and in the thermodynamic limit, the result reads

$$W_{\bar{\rho}_\infty}(A) = \frac{\mathrm{i}}{2\pi} \int_{-\pi}^{\pi} \mathrm{d}k R_k e^{\mathrm{i}k|A|} , \, R_k = \frac{\text{Im}(\tilde{A}_k B_k^*)}{|\tilde{A}_k|^2 + \text{Re}(\tilde{A}_k B_k^*)} ,$$

(H14)

where $\tilde{A}_k = \mathrm{i} e^{\mathrm{i}k} A_k = -e^{\mathrm{i}k} b_k^*$. Let us compute the integral using the contour integral method. We rewrite R_k as a function of $z = e^{\mathrm{i}k}$ as follows

$$R(z) = \mathrm{i}\frac{P_2(z) - \sinh J \sinh h \sqrt{P_4(z)}}{e^J \sinh h(z^2 - 1)} ,$$

$$P_2(z) = 2\sinh J \cosh h z - \cosh J \sinh h(z^2 + 1) ,$$

$$P_4(z) = (z - z_1)(z - z_2)(z - z_3)(z - z_4) , 0 < z_1 < z_2 < 1, z_1 z_4 = z_2 z_3 = 1 .$$

(H15)

(a) Comparision between the exact result of S_A and the approximations

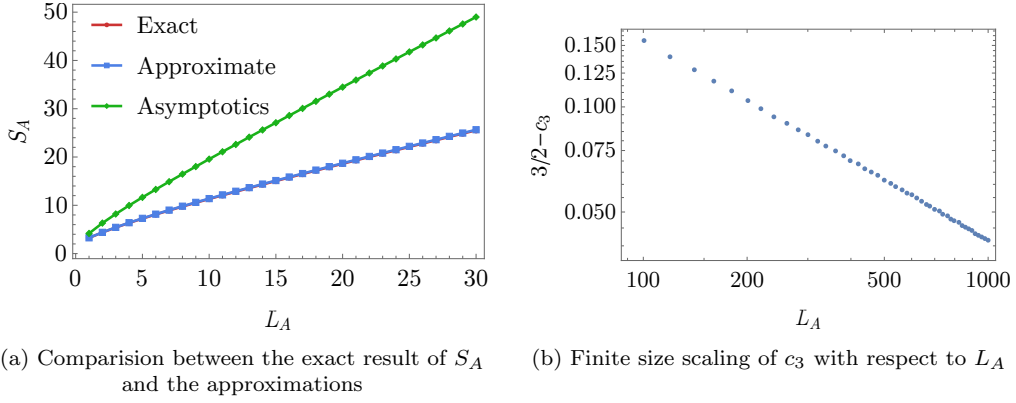(b) Finite size scaling of c_3 with respect to L_A

FIG. 17. (a)Comparison between the exact result of S_A, the approximated result using contour integral and the asymptotic expansion of that. The parameter for the plot is $J = 1, h = 2/5$. The constant C is chosen as $\frac{\sqrt{(z_3 - \bar{z})(z_4 - \bar{z})}}{1 - \bar{z}^2}$ with $\bar{z} = \frac{z_1 + z_2}{2}$ being the middle point of the integration range. (b) We generate the entanglement data using Eq. (H19), fit it by $c_1 + c_2|A| + c_3 \log |A|$ and study c_3's dependence on $|A|$. It can be seen that c_3 exponentially converges to $3/2$ as predicted by Eq. (H22).

$P_4(z)$ is a four-th order polynomial with two of its zeros sitting inside the unit circle and the other two sitting outside. When writing $\sqrt{P_4(z)}$, we implicitly define the two branch cuts to be $[z_1, z_2]$ and $[z_3, z_4]$ so that one is inside and the other one is outside the contour. The whole integral can be written as

$$W_{\bar{\rho}_\infty}(A) = \frac{i}{2\pi} \oint_{|z|=1} dz \frac{P_2(z) - \sinh J \sinh h \sqrt{P_4(z)}}{e^J \sinh h(z^2 - 1)} z^{|A|-1} . \tag{H16}$$

Inside the contour, the integrand does not have any pole but the branch cut $[z_1, z_2]$. By the Cauchy's integral theorem, we can deform the contour to enclose only the branch cut $[z_1, z_2]$. Along the deformed contour, $P_2(z)$ is analytical and thus can be ignored. We have $\arg(z - z_1) = 0, \arg(z - z_2) = \arg(z - z_3) = \arg(z - z_4) = \pi$ above the branch cut and $\arg(z - z_1) = 0, \arg(z - z_2) = \arg(z - z_3) = \arg(z - z_4) = -\pi$ below the branch cut. Consequently, we can convert the contour integral to the following ordinary integral

$$W_{\bar{\rho}_\infty}(A) = \frac{\sinh J}{\pi e^J} \int_{z_1}^{z_2} dx \frac{\sqrt{(x - z_1)(z_2 - x)(z_3 - x)(z_4 - x)}}{1 - x^2} x^{|A|-1} . \tag{H17}$$

When the system is deep in the volume-law phase, $J \gg 1 \gg h$, $z_1 \ll z_2 \ll 1$ and the $(z_3 - x)(z_4 - x)$ and $1 - x^2$ factors are both of order $\mathcal{O}(1)$ during the whole integral. Therefore, we approximate them by a constant, which can be fixed by comparing with the exact result, namely

$$W_{\bar{\rho}_\infty}(A) \approx \frac{\sinh J}{\pi e^J} C \int_{z_1}^{z_2} dx \sqrt{(x - z_1)(z_2 - x)} x^{|A|-1} . \tag{H18}$$

The rest of integral is the hypergeometric function. Recalling the Euler's formula, we have

$$W_{\bar{\rho}_\infty}(A) = \frac{\sinh J \, z_1^{|A|} z_2}{4 e^J |A|(|A| + 1)} C \left[\left(1 + \frac{z_1}{z_2}\right) F\left(-\frac{1}{2}, 1 - |A|, 1, 1 - \frac{z_2}{z_1}\right) \right.$$
$$\left. - \left((1 + 2|A|) + (1 - 2|A|)\frac{z_2}{z_1}\right) F\left(\frac{1}{2}, 1 - |A|, 1, 1 - \frac{z_2}{z_1}\right) \right] . \tag{H19}$$

This provides a good approximation to the exact result, as is shown in Fig. 17. To compute the large $|A|$ expansion of the above expression, we need the asymptotic expansion of the hypergeometric function $F(\alpha, \beta; \gamma; z)$ with respect to a large positive β. Let us recall the definition of (Gaussian) Hypergeometric functions

$$F(\alpha, \beta; \gamma; z) = \sum_{n=0}^{\infty} \frac{(\alpha)_n (\beta)_n}{(\gamma)_n} \frac{z^n}{n!} , \quad (a)_n = \frac{\Gamma(a + n)}{\Gamma(a)} . \tag{H20}$$

If we assume the expansion is interchangable with the infinite sum, then $(\beta)_n$ can be replaced with its large β expansion which leads to

$$F(\alpha, \beta; \gamma; z) \sim \sum_{n=0}^{\infty} \frac{(\alpha)_n}{(\gamma)_n} \frac{(\beta z)^n}{n!} = M(\alpha, \gamma; \beta z), \tag{H21}$$

where $M(a, b; z)$ is the confluent hypergeometric function. As a result, the large parameter expansion of $F(\alpha, \beta; \gamma; z)$ can be reduced to the large argument expansion of $M(a, b; z)$ and we have

$$W_{\bar{\rho}_\infty}(A) \approx \frac{\sinh J \, z_2}{2e^J \sqrt{\pi}} \, C \left(\frac{z_2}{z_1} - 1\right)^{1/2} z_1^{|A|} e^{(1-z1/z2)|A|} |A|^{-3/2}, \tag{H22}$$

The behavior of Eq. (H22) is also plotted in Fig. 17(a) as a comparison. The discrepancy only comes from the inaccurate exponential factor in Eq. (H22) while the power-law factor turns out to be true as verified in Fig. 17(b) as well as in the main text.